Journal of Cleaner Production 315 (2021) 128102

Contents lists available at ScienceDirect

Journal of Cleaner Production

journal homepage: www.elsevier.com/locate/jclepro

Adaptive energy management strategy for sustainable voltage control of PV-hydro-battery integrated DC microgrid

K. Raghavendra Naik [a], Bhooshan Rajpathak [a], Arghya Mitra [a], Mohan Lal Kolhe [b,*]

[a] Department of Electrical Engineering, Visvesvaraya National Institute of Technology, Nagpur, 440010, India
[b] Faculty of Engineering and Science, University of Agder, PO Box 422, NO 4604, Kristiansand, Norway

ARTICLE INFO

Handling editor: Cecilia Maria Villas Bôas de Almeida

Keywords:
DC Microgrid
Small hydro power plant
Solar PV
Adaptive energy management strategy
Sustainable voltage control
Adjustable energy controller

ABSTRACT

DC microgrid has relatively more advantages of power quality, not requirement of reactive power, higher operational efficiency compare to AC microgrid. DC microgrid can facilitate effective integration of distributed clean energy resources and efficient solution for providing electricity to remote areas (e.g. North Eastern States of India). Recently, India has commissioned small hydro, solar PV and battery storage integrated DC microgrids (MGs) to meet the locally increasing load demand of northeastern states. The sudden change in solar insolation during the load power dynamics can cause unbalanced power flow in such isolated MGs. Due to the slow response time of small hydro power plant (SHPP) and limited output power of battery storage with fixed C-rate, the unbalanced power flow, during load power dynamics, cannot be compensated. The unbalanced power flow may lead to unsustainable voltage control at the DC bus of MG. To prevent this, MG follows load shedding. But, load shedding reduces the reliability of MG. To achieve the sustainable voltage control of DC MG, a smart adaptive energy management strategy (AEMS) is proposed in this research work. The novel aspect of proposed AEMS is that it operates the SHPP despite its slow response time by estimating the load power dynamics on the iterative basis. The deep charging/deep discharging scenario of battery storage due to mismatch between the total generation with estimated load and the actual load is taken care by the adjustable energy controller of proposed AEMS. To justify the potential contributions of proposed AEMS, it is assessed against various dynamic test load cases. Based on the assessment of obtained results against various test load cases, in this work, a comparative analysis is carried out between the proposed AEMS and the existing control strategies in the literature. The comparative analysis reveals that with the proposed AEMS, voltage sustainability of MG is improved by 22.7% and the utilization factor of SHPP is enhanced by 55.27% with 98.17% reduction in current stress levels of battery storage system. Finally, the proposed AEMS is evaluated in MATLAB/Simulink as well as validated through OPAL-RT real time simulator.

1. Introduction

The northeastern states of India have poor access to electricity due to their remote location from the rest of India. Despite India's 100% rural electrification in 2018, only 53% of rural villages in north eastern states (NESs) have access to electricity (Central Statistics Office, 2019). To enhance the electricity access in NESs, India has geared up installing large no. of renewable energy based power plants at various places in NESs (Dikshit and Dikshi, 2014). But, the power shortage data of NESs presented in Table 1 reveals that the rate at which the generation capacity increasing is marginally less than the rate at which the peak load demand has been increasing.

Due to abundant potential and large accessibility, integrated operation of solar PV and small hydro based renewable power sources interfaced with the advanced power electronic technology is the best suitable solution to meet the rural electrification and peak load shortage objectives of NESs (Padmanathanet al., 2019). But, due to the environmental concerns over construction of large no. of SHPPs in NESs, the rate of installation of SHPP/year is relatively less than the rate of installation of solar PVs/year as shown in Fig. 1(a).

The economic feasibility studies presented in (Kalita et al., 2019) reveals that installation of solar PVs at various locations in NESs reduces the cost of per unit electricity generation in those regions. This is shown in Fig. 1(b).

But, due to the geographical location of NESs near Tropic of Cancer,

* Corresponding author.
E-mail address: Mohan.L.Kolhe@uia.no (M.L. Kolhe).

https://doi.org/10.1016/j.jclepro.2021.128102
Received 9 January 2021; Received in revised form 3 June 2021; Accepted 23 June 2021
Available online 30 June 2021

Nomenclature

V_{PV}	Terminal voltage of PV module (V)
I_{PV}	Current carried by PV module (A)
$V_{PV}^{'}$	Small change in V_{PV}
I_{SC}	Short circuit current (A)
L_{PV}	Line inductance of solar PV module P_{PV} = Solar PV power output
Y	Solar irradiance (Watt/m^2)
N_S	No. of PV panels in series alignment
N_P	No. of PV panels in parallel alignment
a	Ideal factor
T	Absolute temperature (Kelvin)
K_T	Boltzmann constant (Joule/Kelvin)
q	Charge of electron (Coulomb)
I_0	Reverse saturation current (A)
C_{dc}	DC link capacitance (F)
R_L	DC load (Ω)
V_{MPP}	Voltage tracked by MPPT algorithm
$d_{pv}^{'}$	Small change in duty cycle of
DC-DC	converter interfaced with solar PV
ΔH_t	Change in head at the turbine gate
K_u	Proportional constant
H_{t0}	Hydraulic head at no load (m)
G_t	Ideal gate opening
g_t	Real gate opening
G_{t0}	Ideal gate opening at no load
g_{t0}	Real gate opening at no load
U_t	Water velocity at rated load (m/s)
U_{t0}	Water velocity at no load (m/s)
ρ	Density of water (kg/m3)
L_t	Length of penstock (m)
A_{area}	Cross sectional pipe area
A_{tg}	Turbine gain
D_T	Droop gain of governor
a_g	Acceleration of gravity (m/s^2)
K_{PL}, K_{GM}	Pilot and gate servo gains
K_{PH}	Proportional constant of governor
K_{Ih}	Integral constant of governor
K_{SH}	Proportional gain constant of PMSG
V_{gd}	Equivalent $d-$ axis stator voltages of PMSG
V_{gq}	Equivalent $q-$ axis stator voltages of PMSG
L_{gd}	Equivalent $d-$ axis stator inductances of PMSG (mH)
L_{gq}	Equivalent $q-$ axis stator inductances of PMSG (mH)
$I_{gd} = d-$	Axis line current of PMSG
$I_{gq} =$ q $-$	Axis line current of PMSG
ϕ_m	Flux linkage of PMSG (Web)
B	friction coefficient
J	moment of inertia (kg-m^2)
T_{eg}	Electromagnetic torque of PMSG (N-m)
T_{mech}	Mechanical torque developed by turbine (N-m)
ω_{mc}	Mechanical speed of PMSG (rad/s) P_{mg} = Mechanical power developed by PMSG
D_{SH}	Duty cycle of DC-DC converter interfaced with PMSG
V_{eg}	Stator voltage of PMSG
P_{SHPP}	Output power of SHPP
P_{SHPPRF}	Reference power set by the AEM
P_{adJ}	Adjusted power output set by the AEC
K_{PVB}	Proportional constant of VC
K_{PDB}	Proportional constants of CC
K_{IvB}	Integral constant of VC
K_{IDB}	Integral constant of CC
L_B	Line inductance of BSS
D_{BBS}	Duty cycle of BSS
T_{SEMS}	Response time of AEC (s)
C_{DC}	DC bus capacitance (F)
V_{dc}	Voltage at the DC bus of MG (V)
K	Iteration count
Seconds-'s'	
V_{dcrf}	Reference DC bus voltage (V)
ΔP	Unbalanced load power

Table 1
Peak power shortage scenario in NESs (Executive Summary on Powe, 2018; Executive Summary on Powe, 2019; Executive Summary on Powe, 2020).

	As of Sept. 2018	As of Sept. 2019	As of Sept. 2020
Peak power available (MW)	2850	3070	3104
Peak power demand (MW)	2921	3183	3271
% Deficient peak power	2.4	3.6	5.3

they undergo drastic climate change and this climate change has an impact on solar insolation (Yuan et al., 2020). Therefore, integrated operation of solar PV-small hydro-battery storage as a MG is going to solve the power shortage scenario of NESs.

To electrify the remote community such as NESs, type of MG (AC or DC) plays a significant role. Since, type of MG affects the reliability, stability and economic feasibility of MG (Sadanala et al., 2020). Due to the involvement of less no. of AC-DC and DC-AC conversion stages and simple control structure, DC MGs have more reliability and stability compared to AC MGs (Sadanala and Singh, 1109). Moreover, wide range of applications such as DC homes, LEDs, variable speed drives and electric vehicle charging stations have made the DC MG more popular solution for remote electrification of NESs than AC MG (Sadanala and Singh, 1007). However, attaining sustainable voltage control of hybrid DC MGs due to rapid change in solar insolation during load power dynamics is a critical objective and the same is illustrated in the below section.

1.1. Problem definition

The sudden fall in solar insolation due to unconditional weather during load power dynamics cause unbalanced power flow in the DC MGs (Reddy and Singh, 2018). Due to slow response time of SHPP (8–10s), it cannot compensate the unbalanced power flow instantly (Naik et al., 2021). Moreover, due to the provision on charging and discharging current limit with fixed C-rate, battery storage cannot compensate the unbalanced power flow during load power dynamics (Manandharet al., 2019). The uncompensated load power due to the non-operation of SHPP and limited output power of battery storage system (BSS) may lead to unsustainable voltage control of hybrid DC MG (Al-Shetwi et al., 2019). Therefore, to prevent the damage caused to the connected load due to the unsustainable voltage control, MG follows load shedding. However, load shedding reduces the reliability and stability of DC MG (Shezan, 2020). Therefore, to achieve the sustainable voltage control of considered DC MG during the abnormal situation (sudden fall in PV power during the load power dynamics), a powerful energy management strategy is inevitable.

1.2. Literature review

The sustainable voltage control of solar PV-SHPP based hybrid MG is achieved using a multi BSS and plug in electrical vehicle technology in (Olatunde et al., 2020a). But, the control strategy adopted in (Olatunde et al., 2020a) has not addressed the issue how the voltage control of hybrid DC MG is going to be affected with sudden fall in solar PV power during load power dynamics (Issue 1). In (Guan et al., 2015), a hierarchical control scheme is proposed to achieve the voltage sustainability of hybrid MG. However, the hierarchical control strategy has not reported the issue 1. A comprehensive power control scheme is adopted in (Yi et al., 2018) to achieve the sustainable voltage control of hybrid MG against the load power dynamics. In (Deshmukh et al., 2020), a fuzzy logic based supervised power management strategy is proposed to achieve the sustainable voltage control of hybrid DC MG. Nevertheless, neither the comprehensive power control scheme proposed in (Yi et al., 2018) nor the supervised power management strategy adopted in (Deshmukh et al., 2020) has addressed the Issue 1.

The bi-directional control algorithm adopted in (Singh et al., 2021) has regulated the DC-link voltage of hybrid MG through charging/discharging control of BSS in such a way that load-generation balance is maintained at any instant of time. But, the bi-directional control algorithm has not addressed the issue; how voltage control of hybrid DC MG is going to be achieved with fixed C-rate of BSS and constant output power from SHPP (Issue 2). The power management strategy reported in (Sharma et al., 2020) has regulated the dc link voltage of islanded hybrid MG (solar PV-hydro-BSS) against the source and load dynamics using BSS control. However, the power management strategy in (Sharma et al., 2020) has not addressed the Issue 2.

The decentralized multi-agent system proposed in (Olatunde et al., 2020b) has improved the voltage profile of hybrid MG through reactive power regulation. However, the proposed multi-agent model has not considered the C-rate limitation and BSS, response time of hydro generator. In (Kewat and Singh, 2019), active power flow control of BSS is used to achieve the sustainable voltage control of hybrid MG against the source and load dynamics. But, due to slow response time of SHPP, the proposed control strategy has kept the SHPP in the constant power mode and let the BSS compensate the load dynamics. Consequently, the power management strategy adopted in (Kewat et al., 2018) has compensated the sudden change in load power and solar PV dynamics through active power control of BSS. The control scheme adopted in (Sharma et al., 2019) has operated the BSS to compensate the power flow oscillations due to source and load dynamics of hybrid MG. Nevertheless, this control scheme is also suffered with issue 2.

The uncompensated load power dynamics due to fixed C-rate limitation of BSS with the active power flow control methods adopted in the aforementioned literature may cause the voltage at the DC bus of MG exceed ±15% V_{dc} limit. The exceeded voltage limit may lead the MG to unstable mode ("Standard for the Sp, 2018).

A collaborative optimization process of energy storage system is established in (Li et al., 2020) to stabilize the MG against the load-generation imbalance due to intermittent solar PV and load dynamics. Nevertheless, the collaborative optimization approach has not considered the C-rate limitation of energy storage system. A Hetero-functional graph theory based energy management strategy is proposed in (Schoonenberg and Farid, 2017) to achieve the voltage sustainability of MG through load-generation balance. But, this strategy has not considered the dynamics of hydro generator. The adaptive control scheme in (Kalla et al., 2018) has attained the sustainable voltage control of hybrid MG through optimal power flow management. However, the adaptive control scheme proposed in (Kalla et al., 2018) has not addressed the Issue 2.

The unbalanced power flow of hybrid MG due to the rapid varying solar PV power output is solved using the active power control model in (Ling et al., 2019). But, the active power control model has not considered the Issue 2. In (Chandran et al., 2020), an imbalanced power flow of MG due to solar PV and load power dynamics are compensated by the BSS. However, the control strategy incorporated in (Yuan, Liu, Su, Wang) has not considered the C-rate limitation of BSS. An iterative trial calculation method is used in (Yuan, Liu, Su, Wang) to mitigate the impact of solar PV dynamics on voltage control of PV-Hydro integrated MG. But, this strategy has not addressed Issue 2.

From the literature review, it is inferred that the control strategies presented in the literature have not explored how the voltage control of solar PV-SHPP-BSS based hybrid MG is going to be achieved against the constraints such as slow response time of SHPP, C-rate limitation of BSS and sudden fall in solar PV power during the load power dynamics. However, despite the aforementioned constraints, the proposed AEMS ensures the sustainable voltage control of hybrid MG through a load estimation algorithm and adjustable energy controller (AEC). The load estimation algorithm of AEMS generates a reference power to SHPP on iterative basis and ensures that SHPP compensates the load power dynamics despite its slow response time. Consequently, AEC adjusts the output power of SHPP in such a way that BSS does not exceed its maximum storage capacity limit with reference to C-rate while compensating the mismatch between the actual load power and estimated load power delivered by the SHPP. The novel contributions of proposed AEMS are given below.

1. Despite the slow response time and hammering effect limitations, AEMS should operate the SHPP during the abnormal situation.

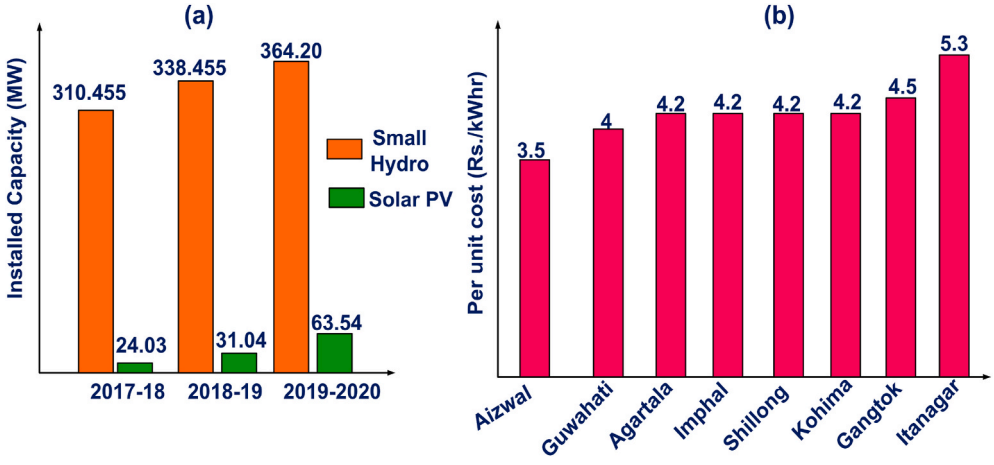

Fig. 1. (a) Installed capacity of small hydro and solar PV in north east India, (b) Cost/unit with solar PV generation (Kalita et al., 2019).

2. Adjustable energy controller of AEMS should ensure the power compensated by the BSS in charging/discharging mode does not exceed its maximum storage capacity with reference to C-rate limit.
3. The proposed AEMS should maintains the sustainable voltage control of DC MG against the sudden rise and fall in load power demand during peak and non-peak load condition. The control strategies in the existing literature are not validated against such load patterns.
4. To compensate the load power dynamics about peak load condition with the existing control strategies in literature, large size BSS should be incorporated. But, the proposed AEMS should compensate the load power dynamics with reduced sizing of BSS.
5. The proposed AEMS should ensure reduced current stress levels and enhanced battery life due to utmost utilization of SHPP during the load power dynamics.

The proposed research work is organized into seven sections. Section 2 illustrates the configuration and modeling of solar PV-SHPP-battery storage integrated DC MG. Section 3 explains adaptive energy management strategy. Section 4 presents the MATLAB/Simulink results of proposed strategy. Section 5 demonstrates the real time validation of proposed strategy in OPAL-RT. Section 6 discusses the comparative analysis. Finally, section 7 is going to present the conclusion and future scope of proposed research work.

2. Configuration and modeling of solar PV-SHPP-battery storage integrated DC MG

The solar PV-SHPP-battery storage integrated DC MG is a feasible solution to meet the rural electrification and power shortage scenario of NESs from economic and clean energy perspective (Cortés et al., 2020). Moreover, the DC MG structure shown in Fig. 2 is more suitable for contemporary loads such as LEDs, electric vehicles, charging stations, dynamic loads etc. (Ullah et al., 2020).

The SHPP shown in Fig. 2 is using semi Kaplan turbine. The semi Kaplan turbine sets the required mechanical input (P_{Mech}) to the coupled permanent magnet synchronous generator (PMSG) for producing the required electrical power output. The AC power output from SHPP is converted into controlled DC power output by a rectifier and DC-DC converter. The solar PV array dispatch the maximum power output with reference to the available solar insolation. BSS makes the reference DC bus and compensate the unbalanced power flow between the renewable generation (solar PV and SHPP) and dynamic load. The considered PV parameters of the DC MG (Fig. 2) is given in the Table 2, and the remaining used technical specifications / parameters of the DC MG are given in the Appendix I.

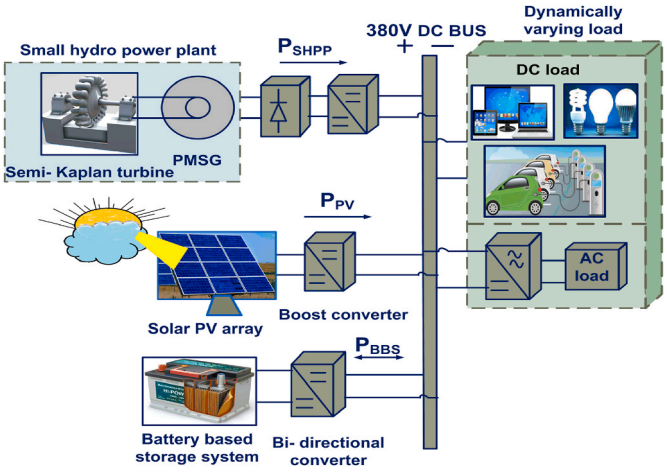

Fig. 2. Block diagram of SH-SPV-BSS based DC MG.

Table 2
Design parameters of solar PV system.

P_{PV} per panel	V_{PV} and I_{PV} per panel	N_S&N_P	Total array's V_{PV} & I_{PV}	PV power capacity
270W	31.1 V & 8.67A	8 &17	256 V & 156.25 A	40 kW

2.1. Smart aspects of MG

The augmentation of smart grid concept into the PV- small hydro-BSS based MGs enhances the reliability, sustainability and stability of such MGs (da Silva et al., 2020). As per (Microgrids, 2017), a smart MG is one which makes the intelligent coordination among the various distributed energy sources and loads of the MG through an area based communication network. The smart aspects of MG are given as follows.

1. Maximum utilization of intermittent source (solar PV) and optimal utilization of main dispatchable source with smart energy management strategy improves the stability as well as efficiency of MG.
2. Reduced environmental pollution with clean energy production.
3. Optimal scheduling and smart management of renewable sources during peak and non-peak load condition by taking into account the source constrains such as intermittency of solar insolation, change in rate of water flow discharge of SHPP and state of charge of BSS improves the economic feasibility and reliability of MG.

2.2. Modeling of solar PV system

Solar PV system modeling includes PV array and boost converter with maximum power point tracking (MPPT) algorithm as shown in Fig. 3. In this work, incremental conductance/hill climbing MPPT algorithm given in (Sharma et al., 2019) is used to extract the maximum power from solar PV array.

The current through solar PV array is given as follows (Liet al, 2019)

$$I_{PV} = N_P I_{SC}\left(\frac{Y}{Y_{ref}}\right) - N_P I_0\left(e^{\left(\frac{qV_{PV}}{aK_T N_S T}\right)} - 1\right) \tag{1}$$

Power available across the PV terminals is

$$P_{PV} = V_{PV}\left(N_P I_{SC}\left(\frac{Y}{Y_{ref}}\right) - N_P I_0\left(e^{\left(\frac{qV_{PV}}{aK_T N_S T}\right)} - 1\right)\right) \tag{2}$$

The operation of boost converter can be depicted using the following equations (Kesilmiş et al., 2020)

$$\frac{dI_{PV}}{dt} = \frac{V_{PV}}{L_{PV}} - \frac{(1-d_{pv})}{L_{PV}} \tag{3}$$

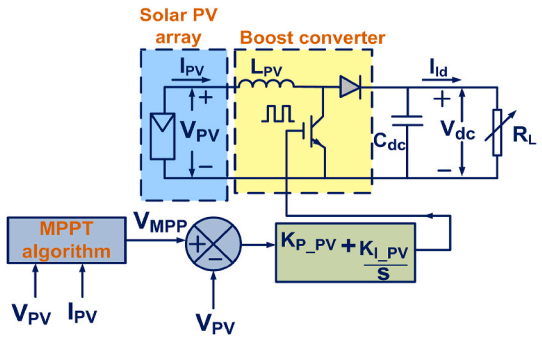

Fig. 3. Control block diagram of solar PV system (Kewat et al., 2018).

$$\frac{dV_{dc}}{dt}=\frac{I_{PV}\left(1-d_{pv}\right)}{C_{DC}}-\frac{V_{dc}}{R_{ld}C_{DC}} \tag{4}$$

The small signal model of boost converter is given as follows

$$\frac{V_{dc}^{'}}{V_{PV}^{'}}=\frac{\left(1-d_{PV}^{'}\right)}{L_{PV}C_{DC}s^{2}+\frac{L_{PV}}{R_{L}}s+\left(1-d_{PV}^{'}\right)^{2}} \tag{5}$$

$$P_{PV}=V_{PV}\times I_{PV} \tag{6}$$

With reference to the change in solar insolation, the duty cycle d_{pv} of boost converter is going to be adjusted by the PI controller corresponding to the error$(V_{MPP}-V_{PV})$ as shown in Fig. 3. Eq. (4) describes this operation.

2.3. Modeling of small hydro power plant

The modeling of SHPP includes semi Kaplan turbine, PMSG, rectifier and DC-DC converter. The PI based governor shown in Fig. 4(a) is equipped with a pilot servo system and gate servo system to regulate the flow rate and gate position of valve as shown in Fig. 4(a). Once, the governor sets the required flow rate then with reference to Eq. (12) semi-Kaplan turbine delivers the required mechanical power to the PMSG.

Semi Kaplan turbine is an axial flow turbine with movable blades. It is optimally suitable for SHPP due to decent efficiency (92–93%) with low and medium head (1.5m–20m) applications. Moreover, due to wide operating range of flow rate (3–30 m^3/s), it can be employed for mini, micro hydro generator application as well. The overall cost of SHPP with Semi-Kaplan turbine for rural electrification is much cheaper than the large hydro project due to non-requirement of large dams and storage tanks (Comino et al., 2020). The hydraulic to mechanical power conversion of semi-Kaplan turbine can be understand with the following equations deduced from the non-linear hydro turbine model shown in Fig. 4(a).

The rotational water velocity of hydro turbine is (Yuan, Liu, Su, Wang)

$$U_t=K_uG_t\sqrt{H_t} \tag{7}$$

Water discharge rate is

$$Q_t=A_{area}\times U_t \tag{8}$$

The mechanical power developed by the hydro turbine is

$$P_{mech}=H_t(U_t-U_{t0}) \tag{9}$$

The incremental pressure change in the penstock is given by

$$\rho a_g\Delta H_t=-\left(\rho L_tA_{area}\frac{dU_t}{dt}\right) \tag{10}$$

$$\frac{\Delta H_t}{\Delta G_t}=\frac{-sT_{wt}}{1+sT_{wt}} \tag{11}$$

$$\frac{g_t}{\Delta P_{SHPP}}=\frac{K_{PL}(K_{PH}s+K_{Ih})}{s^2T_{PL}+s(K_{PH}K_{PL}D_T+1)+K_{Ih}K_{PL}D_T}\left(\frac{K_{GM}}{1+sT_{GM}}\right) \tag{12}$$

where,

$$U_{t_0}=A_tg_{t_0}\sqrt{H_{t_0}},A_t=\frac{G_t}{g_t},T_{wt}=\frac{L_tU_t}{a_gH_t}$$

2.3.1. Modeling of PI based electronic governor

The following control equations are derived for designing PI based electronic governor shown in Fig. 4 (a) to ensure the stability of hydro turbine-PMSG system. The simplified control block diagram shown in Fig. 4(b) is derived from the hydro turbine-governor model given in Fig. 4(a). A and B in Fig. 4(b) are given as follows

$$A=\frac{K_{PL}(K_{PH}s+K_{Ih})}{s(1+sT_{PL})+D_P(K_{PL}(K_{PH}s+K_{Ih}))},B=\frac{K_{SH}K_{GM}(1-sT_{wt})}{(1+sT_{GM})(1+0.5\times sT_{wt})(1+sT_{MS})}$$

The transfer Function of simplified model shown Fig. 4(b) is given as follows

$$\frac{P_{SHPP}}{P_{SHPPRF}\pm P_{adJ}}=\frac{(s^2N_{m1}+sN_{m2}+N_{m3})}{(s^5D_{n1}+s^4D_{n2}+s^3D_{n3}+s^2D_{n4}+sD_{n5}+D_{n6})} \tag{13}$$

where,

$$D_{n1}=T_{PL}\frac{T_{wt}}{2}T_{MS},\ D_{n2}=\left(\frac{T_{wt}}{2}T_{MS}+T_{GM}T_{MS}+T_{GM}\frac{T_{wt}}{2}\right)T_{PL}+\frac{T_{wt}}{2}T_{MS}$$

$$D_{n3}=K_{PL}K_{Ih}D_P\frac{T_{wt}}{2}T_{MS}+T_{PL}T_{MS}+\frac{T_{wt}}{2}T_{PL}+T_{GM}T_{PL}+(K_{PL}K_{PH}D_P+1)\left(\frac{T_{wt}}{2}T_{MS}+T_{GM}T_{MS}+T_{GM}\frac{T_{wt}}{2}\right)$$

$$D_{n4}=K_{PL}K_{Ih}D_P\left(\frac{T_{wt}}{2}T_{MS}+T_{GM}T_{MS}+T_{GM}\frac{T_{wt}}{2}\right)+(K_{PL}K_{PH}D_P+1)\left(\frac{T_{wt}}{2}+T_{MS}+T_{GM}\right)+T_{PL}-K_{SH}K_{GM}T_{wt}$$

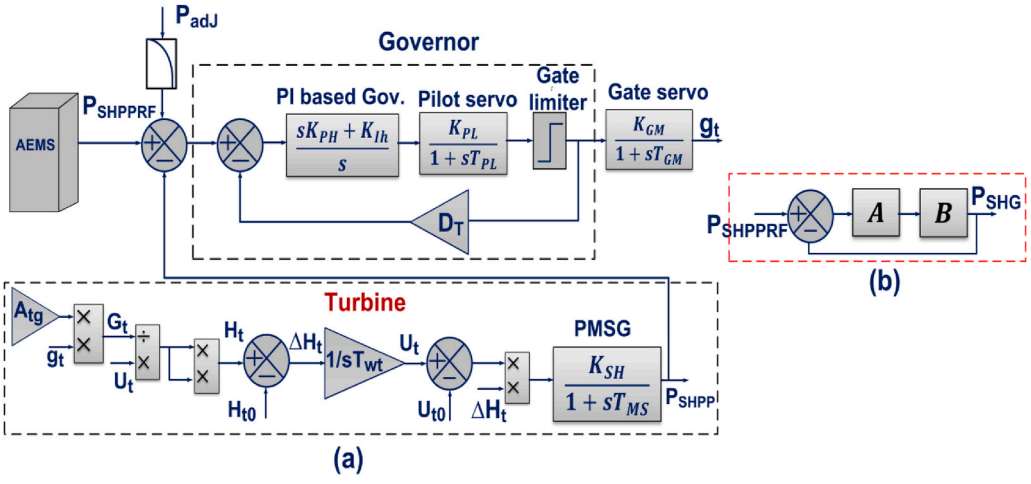

Fig. 4. (a) Control diagram of hydro turbine model (b) simplified block diagram of hydro turbine.

$$D_{n5}=K_{PL}K_{Ih}D_P\left(\frac{T_{wt}}{2}+T_{MS}+T_{GM}\right)+K_{PL}K_{PH}D_P+K_{PL}K_{PH}-K_{PL}K_{Ih}K_{SH}K_{GM}T_{wt}+1$$

$$D_{n6}=K_{PL}K_{Ih}D_P+K_{PL}K_{Ih}K_{SH}K_{GM}$$

$$N_{m1}=-K_{SH}K_{GM}T_{wt},\ N_{m2}=K_{PL}K_{PH}-K_{PL}K_{Ih}K_{SH}K_{GM}T_{wt},\ N_{m3}=K_{PL}K_{Ih}K_{SH}K_{GM}$$

The P_{SHPPRF} in Fig. 4(a) is set by the AEMS and based on the output power of SHPP, PI based governor is going to set gate opening g_t in such a way that$P_{SHPPRF}=P_{SHPP}$. The droop gain (D_T) shown in Fig. 4(a) is going to be adjusted corresponding to the output power of SHPP. 5% change in D_T leads the SHPP to deliver 100 kW to the load. By keeping in mind the slow response time (8.5s) and hydro turbine stability, the PI based governor is designed with a gain margin of 8.78 dB at 0.656 rad/s and phase margin of 134° at 0.156 rad/s as shown in Fig. 5. The controller parameters of governor corresponding to the designed GM and PM are $K_{PL}=0.695$ and $K_{Ih}=0.109$.

2.3.2. PMSG modeling

The following equations depict the modeling of PMSG (Borkowski, 2018)

$$V_{gd}=I_{gd}R_g+L_{gd}\frac{dI_{gd}}{dt}-\omega_{eg}L_{gq}I_{sq} \tag{14}$$

$$V_{gq}=I_{gq}R_g+L_{gq}\frac{dI_{gq}}{dt}+\omega_{eg}L_{gd}I_{gd}+\omega_{eg}\phi_m \tag{15}$$

The equivalent electrical power developed by PMSG in d-q ref. frame can be expressed as

$$P_{mg}=\frac{3}{2}\omega_{eg}\phi_m I_{gq}=\frac{3}{2}\frac{p}{2}\omega_{mc}I_{gq}\phi_m \tag{16}$$

The mechanical equation of SHPP is

$$T_{mech}=T_{eg}+B\omega_{eg}+J\frac{d\omega_{mc}}{dt} \tag{17}$$

To simplify the SHPP model, response time should be incorporated in Eq. (17). Henceforth, modified mechanical equation of SHPP is given as

$$T_{RS}\left(\frac{P_{mg}}{\omega_{eg}^2}\right)\frac{d\omega_{mc}}{dt}=T_{mech}-T_{eg} \tag{18}$$

The total response time of SHPP is. $(T_{RS})=T_{wt}+T_{GM}+T_{PL}+T_{MS}=8.5$ sec

Water time constant$T_{wt}=1$ sec, Gate servo time constant $T_{GM}=1.2$ sec.

Pilot servo time constant $T_{PL}=0.05$ sec, Time constant of rotor and turbine runner. $T_{MS}=6.5s$

2.3.3. Rectifier and DC-DC converter modeling

To dispatch the power flow from SHPP proportional to the reference DC bus voltage, the PI controller in Fig. 6 is going to set a duty cycle for DC-DC converter in such a way that the reference current proportional to P_{SHPPRF} set by the AEM exactly matches the current delivered by DC-DC converter interfaced with PMSG.

The following equations demonstrate the brief modeling of power conditioning devices (AC/DC and DC-DC). The DC output voltage of bridge rectifier is

$$V_{drec}=\frac{3\times\sqrt{2}}{\pi}V_{eg} \tag{19}$$

The output current of DC-DC converter is

$$I_{gdc2}=\frac{I_{gdc1}}{D_{SH}} \tag{20}$$

Equivalent DC output power of SHPP is

$$P_{SHPP\_dc}=\frac{(K_{PDC}s+K_{IDC})}{s}\left(\frac{P_{SHGRF}}{V_{drec}}-I_{gdc2}\right)V_{drec}\times I_{gdc2} \tag{21}$$

By neglecting conversion losses

$$P_{SHPP}=P_{SHPP\_dc} \tag{22}$$

I_{gdc1}, I_{gdc2} = Output currents of bridge rectifier and DC-DC converter.

2.4. Modeling of battery storage system

The BSS consists of a Lithium-ion battery and a bidirectional DC-DC

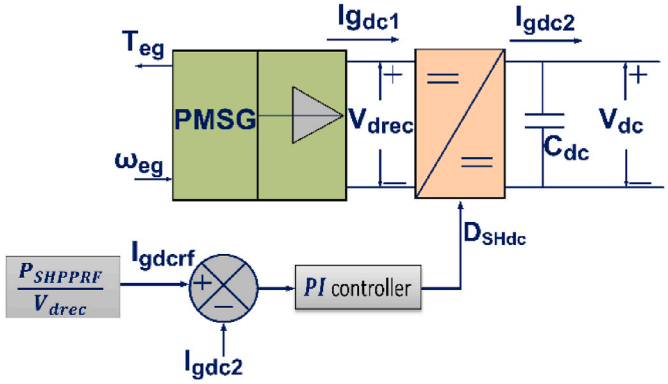

Fig. 6. Block diagram of power conditioning devices of SHPP.

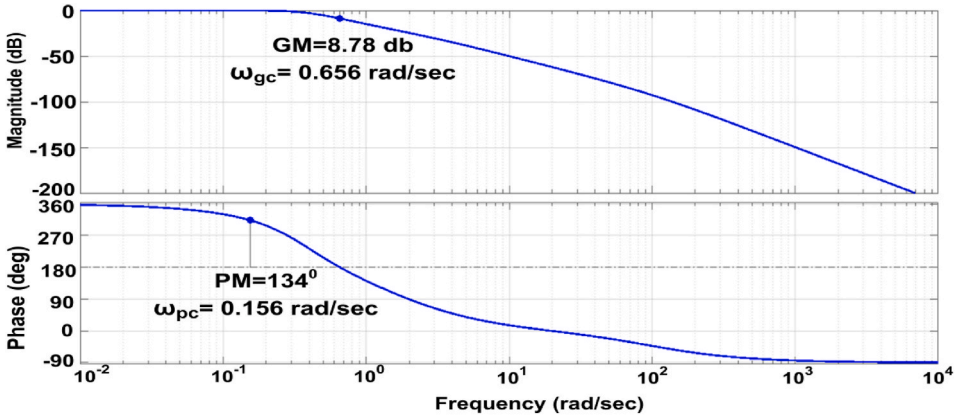

Fig. 5. Frequency response of hydro turbine transfer function model.

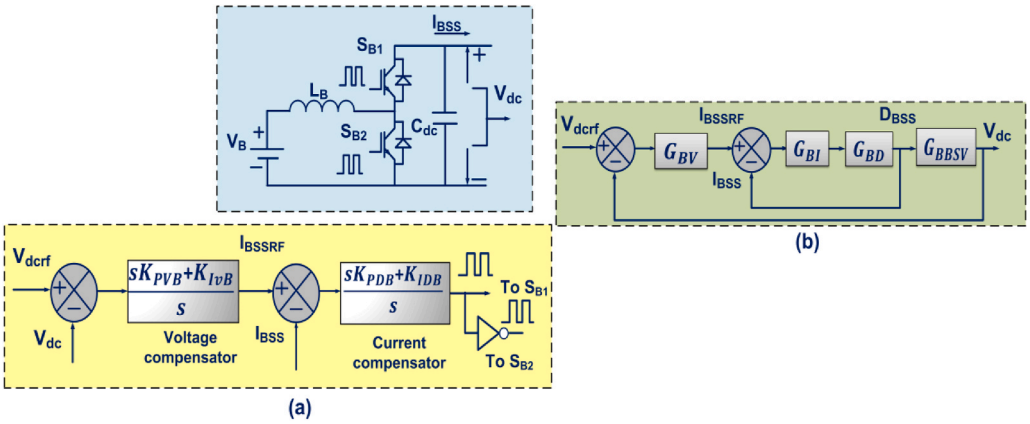

Fig. 7. (a) Block diagram of BSS (b) Equivalent closed loop control diagram of BSS.

converter. The role of BSS control strategy shown in Fig. 7 is that it maintains the constant voltage at the DC bus of MG by compensating the unbalanced power flow between SHPP and load power dynamics. The following equations reveal how BSS is going to regulate the voltage at the DC bus of MG through power flow balancing mechanism.

$$V_{dcrf}C_{dc}\frac{dV_{dc}(t)}{dt} = P_{SHPP}(t) - P_L(t) \pm P_{BSS}(t) \tag{23}$$

$$\frac{dV_{dc}(t)}{dt} = \frac{P_{SHPP}(t) - P_L(t) \pm P_{BSS}(t)}{V_{dcrf}C_{dc}} \tag{24}$$

If the magnitude of unbalanced power flow then bi-directional converter shown in Fig. 7(a), is going to operate in the buck mode with switch S_{B1} turns on.

If $P_{PV} + P_{SHPP} - P_L = -\Delta P$, then bi-directional converter is going to operate in boost mode with switch S_{B2} turns on. Based on the error between V_{dcrf} and V_{dc} due to ΔP, the PI based voltage compensator (VC) shown in Fig. 7(a) is going to set the reference current I_{BSSRF} in such a way that $V_{dcrf} = V_{dc}$. The PI based current compensator (CC) in Fig. 7(a) is going to adjust the duty cycle of bi-directional converter in such a way that. $I_{BSS} = I_{BSSRF}$.

The block diagram representation of aforementioned control strategy is shown in Fig. 7(b). To test the importance of incorporating VC and CC in Fig. 7(b), a step change in R_L is applied. From Fig. 8 (a) and (b), it is observed that for a step change in R_L from 30Ω to 20Ω, voltage control loop (VCL) without compensator (G_{BBSV}) has become unstable with a gain margin (GM) and phase margin (PM) of − 0.87 dB & infinite respectively.

But, VCL with compensator (G_{BV_CP}) is stable with a GM & PM of 8.46 dB and 52.9°. In this work, VCL and current control loop (CCL) are designed with a PM of 49° occurs at 366 rad/s and 4k rad/s shown in Fig. 8(a). The parameters of VCL and CCL with reference to the designed PM and GM are $K_{PVB} = 0.21$, $K_{IvB} = 93$, $K_{PDB} = 0.04$, $K_{IDB} = 135$.

The open loop transfer function of VCL and CCL shown in Fig. 7(b) are given as follows

$$G_{BV\_CP} = G_{BV} \times G_{BBSV} \times \frac{G_{BI}G_{BD}}{1 + G_{BI}G_{BD}} \tag{25}$$

$$G_{BI\_CP} = G_{BI} \times G_{BD} \tag{26}$$

where,

$$G_{BV} = \frac{1}{s}(K_{PVB}s + K_{IiB}),\ G_{BI} = \frac{1}{s}(K_{PDB}s + K_{IDB}),$$

$$G_{BD} = \frac{V_{dc}}{L_B}\left(\frac{\left(s + \frac{2}{R_L \times C_{dc}}\right)}{s^2 + \frac{s}{C_{dc} \times R_L} + \frac{(1-D_{BBS})^2}{C_{dc} \times L_B}}\right), G_{BBSV} = \frac{R_L(1-D_{BBS}) \times \left(1 - \frac{L_B s}{R_L(1-D_{BBS})^2}\right)}{C_{dc} \times R_L\left(s + \frac{2}{C_{dc} \times R_L}\right)}$$

3. Adaptive energy management strategy (AEMS)

The uncompensated load power dynamics due to the hammering effect, slow response time of SHPP (Chandran et al., 2020), and limited output power of BSS due to fixed C-rate (Naik et al., 2021) may lead to unsustainable voltage control of DC MG. Hence, to attain the sustainable voltage control of considered DC MG amid load power dynamics, the operation of SHPP is very much required despite its slow response time.

The proposed AEMS in this work operates the SHPP despite its slow response time during the abnormal situation through load estimation algorithm. Here, the abnormality refers to fall in solar PV power output P_{PV} below 6 kW during load power dynamics. The adaptive energy manager (AEM) shown in Fig. 9 monitors P_{PV}, P_{BSS} and load power dynamics $P_{LN}, P_{LN+1} \ldots . P_{Ln}$ on iteration basis. If the P_{PV} falls below 6 kW (15% of 40 kW) during load power dynamics then AEM triggers this situation and it generates $P_{SHPPK+1}$ based on the no. of load power dynamics before the abnormality. AEM is going to set the estimated load power $P_{SHPPK+1}$ in each iteration as a reference power (P_{SHPPRF}) to SHPP as shown in Fig. 10. Based on the no. of load power dynamics (N), how AEMS is going to generate $P_{SHPPK+1}$ for each iteration count is given as follows.

If the no. of load dynamics $(N) = 2$ then estimated load is given as

$$P_{SHPPK+1} = P_{LN} + \Delta P'_{L1} \tag{27}$$

where, $\Delta P'_{L1} = |P_{L2} - P_{L1}|$

If the no. of load dynamics $(N) = 3$ then estimated load is

$$P_{SHPPK+1} = P_{LN} + \Delta P'_{LN+1} \tag{28}$$

$$\text{where } \Delta P'_{LN+1} = \left\{ \begin{array}{ll} \left(\frac{|\Delta P_{LN-1} + \Delta P_{L1}|}{N-1}\right) & For\ j = 1 \\ \left(\frac{|\Delta P_{LN-1} - \Delta P_{L1}|}{N-2}\right) & For\ j = 2 \end{array} \right\}$$

$$P_{SHPPK+1} = P_{LN} + \left(\frac{\Delta P_{LN-1} + \Delta P_{L1}}{N-1\ (=2)}\right) + \left(\frac{\Delta P_{LN-1} - \Delta P_{L1}}{N-2(=1)}\right) \tag{29}$$

If the no. of load dynamics $(N) = 4$ then estimated load is

$$P_{SHPPK+1} = P_{LN} + \Delta P'_{LN+1} \tag{30}$$

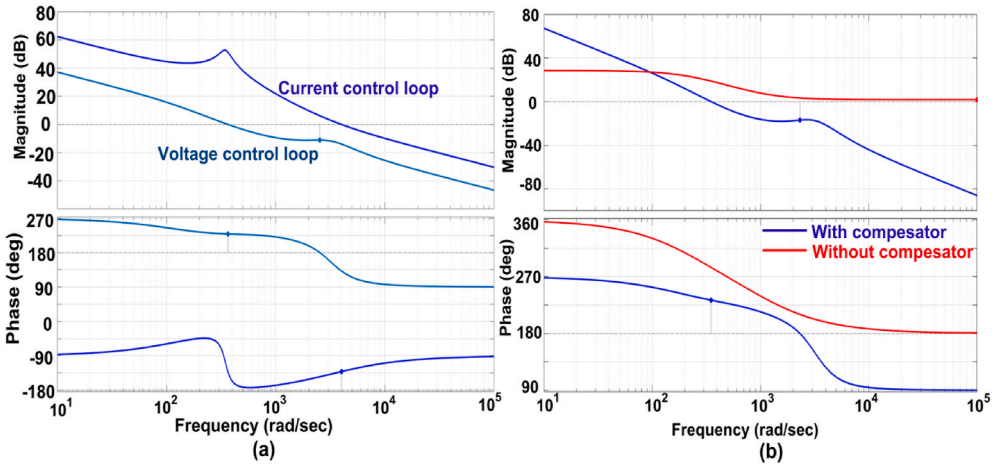

Fig. 8. Bode plot of (a) Voltage and current control loop, (b) VCL with step change in.R_L

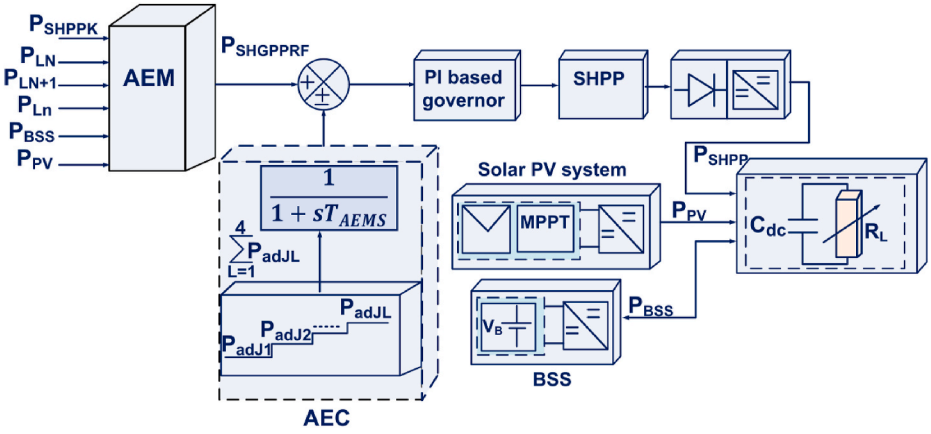

Fig. 9. Block diagram of AEMS.

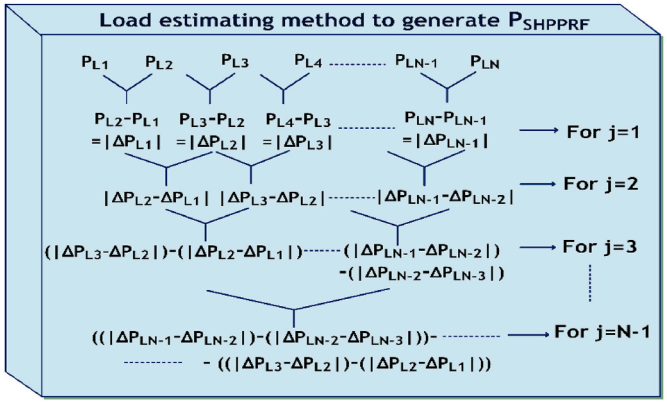

Fig. 10. Estimation of load power for generating reference power to SHPP.

where

$$\Delta P'_{LN+1} = \left\{ \begin{array}{ll} \left(\frac{\Delta P_{L1} + \Delta P_{L2} + \cdots \Delta P_{LN-1}}{N-1}\right) & For\, j = 1 \\ \left(\frac{(|\Delta P_{L2} - \Delta P_{L1}|) + \ldots + (|\Delta P_{LN-1} - \Delta P_{LN-2}|)}{N-2}\right) & For\, j = 2 \\ \left(\frac{|(|\Delta P_{LN-1} - \Delta P_{LN-2}|) - (|\Delta P_{L2} - \Delta P_{L1}|)|}{N-3}\right) & For\, j = 3 \end{array} \right\}$$

For $N > 4$ the estimated load power is

$$P_{SHPPK+1} = P_{LN} + \Delta P'_{LN+1} \tag{32}$$

where

$$P_{SHPPK+1} = P_{LN} + \left(\frac{\Delta P_{L1} + \Delta P_{L2} + \cdots \Delta P_{LN-1}}{N-1}\right) + \left(\frac{(|\Delta P_{L2} - \Delta P_{L1}|) + \ldots + (|\Delta P_{LN-1} - \Delta P_{LN-2}|)}{N-2}\right) + \left(\frac{(|\Delta P_{LN-1} - \Delta P_{LN-2}|) - (|\Delta P_{L2} - \Delta P_{L1}|)}{N-3}\right) \tag{31}$$

$$\Delta P'_{LN+1} = \left\{ \begin{array}{ll} \left(\frac{\Delta P_{L1} + \Delta P_{L2} + \cdots \Delta P_{LN-1}}{N-1}\right) & For\, j = 1 \\ \left(\frac{(|\Delta P_{L2} - \Delta P_{L1}|) + (|\Delta P_{L3} - \Delta P_{L2}|) \ldots + (|\Delta P_{LN-1} - \Delta P_{LN-2}|)}{N-2}\right) & For\, j = 2 \\ \vdots & \\ \frac{((|\Delta P_{LN-1} - \Delta P_{LN-2}|) - (|\Delta P_{LN-2} - \Delta P_{LN-3}|)) - \ldots - ((|\Delta P_{L3} - \Delta P_{L2}|) - (|\Delta P_{L2} - \Delta P_{L1}|))}{N - n(=1)} & For\, j = N - n = 1 \end{array} \right\}$$

$$P_{SHPPK+1} = P_{LN} + \left(\frac{\Delta P_{L1} + \Delta P_{L2} + \ldots \Delta P_{LN-1}}{N-1}\right) + \left(\frac{(|\Delta P_{L2} - \Delta P_{L1}|) + (|\Delta P_{L3} - \Delta P_{L2}|) \ldots + (|\Delta P_{LN-1} - \Delta P_{LN-2}|)}{N-2}\right) + \ldots + \left(\begin{array}{l} \frac{((|\Delta P_{LN-1} - \Delta P_{LN-2}|) - (|\Delta P_{LN-2} - \Delta P_{LN-3}|)) -}{N - n(=1)} - \\ \ldots - \frac{((|\Delta P_{L3} - \Delta P_{L2}|) - (|\Delta P_{L2} - \Delta P_{L1}|))}{N - n(=1)} \end{array} \right) \tag{33}$$

where.

$P_{LN} = N^{th}$ Load power, $\Delta P'_{LN+1}$ = estimated load power change
$P_{SHPPK+1}$ = Estimated load power for the $(K+1)^{th}$ iteration,
n = Integer which represents N^{th} load power at steady state

For instance, if the abnormality occurs at 't' seconds with N no. of load power fluctuations then AEM is going to set a reference power i.e. $P_{SHPP(K=1)+1}$ to SHPP based on Eq. (27). Consequently, in the succeeding iteration (K=K+1), AEM tracks the load dynamics for 't+10'seconds and based on N it is going to set a dispatchable reference power of $P_{SHPPK+1}$ to SHPP as shown in Fig. 10. The step by step procedure of generating $P_{SHPPK+1}$ for each 'K' is shown in Fig. 10. Therefore, through the estimating algorithm shown in Fig. 10 the proposed AEMS operates the SHPP against the abnormal situation. This is the novel aspect of the proposed AEMS that has not been addressed in any of the research works presented in the literature.

During the load estimation, when there is a mismatch between the actual load power and total generation with the estimated load then BSS may get into deep charging/discharging mode. To regulate the power flow of BSS during mismatched load power, proposed AEMS uses the control algorithm shown in Fig. 11. As per the proposed control algorithm of AEMS, if the BSS has reached 80% of P_{BSSmax} either in charging or discharging mode due to the mismatch between actual load power and total generation during any iteration 'K' then AEMS let the AEC adjust the output power of SHPP as per the following equations.

When $P_{BSSK} \geq 0.8|P_{BSSmax}|$ in discharging mode

$$P_{PV}(t) + P_{SHPPK}(t) + P_{adJK}(t) = P_{LN} \tag{34}$$

when $P_{BSSK} \geq 0.8|P_{BSSmax}|$ in charging mode

$$P_{PV}(t) + P_{SHPPK}(t) - P_{adJK}(t) - P_{LN} = 0.5P_{BSSmax} \tag{35}$$

3.1. Modeling of adjustable energy controller

To compensate the mismatched load with reference to the equations given in Eq. (34) & Eq. (35), instead of applying step change in P_{adJ}, AEMS has incorporated distributed proportional change in P_{adJ} as shown in Fig. 9. The transfer function of adjustable energy controller is given as follows

$$P_{adJ} = \frac{1}{X\,(1 + sT_{AEMS})} \sum_{L=1}^{L=4} P_{adJL} \times (X - L + 1) \tag{36}$$

where, X = 4, T_{AEMS} = 0.5s.

In Eq. (36), the distribution of P_{adJ} into $P_{adJ1}, P_{adJ2} \ldots P_{adJ4}$ with a delay time of T_{AEMS} is done to ensure the smooth load power correction without any mechanical transients in the turbine's penstock. Once, the mismatch occurs, AEM is going to stop operating the SHPP through load estimating algorithm, rather, it operates the SHPP through AEC as

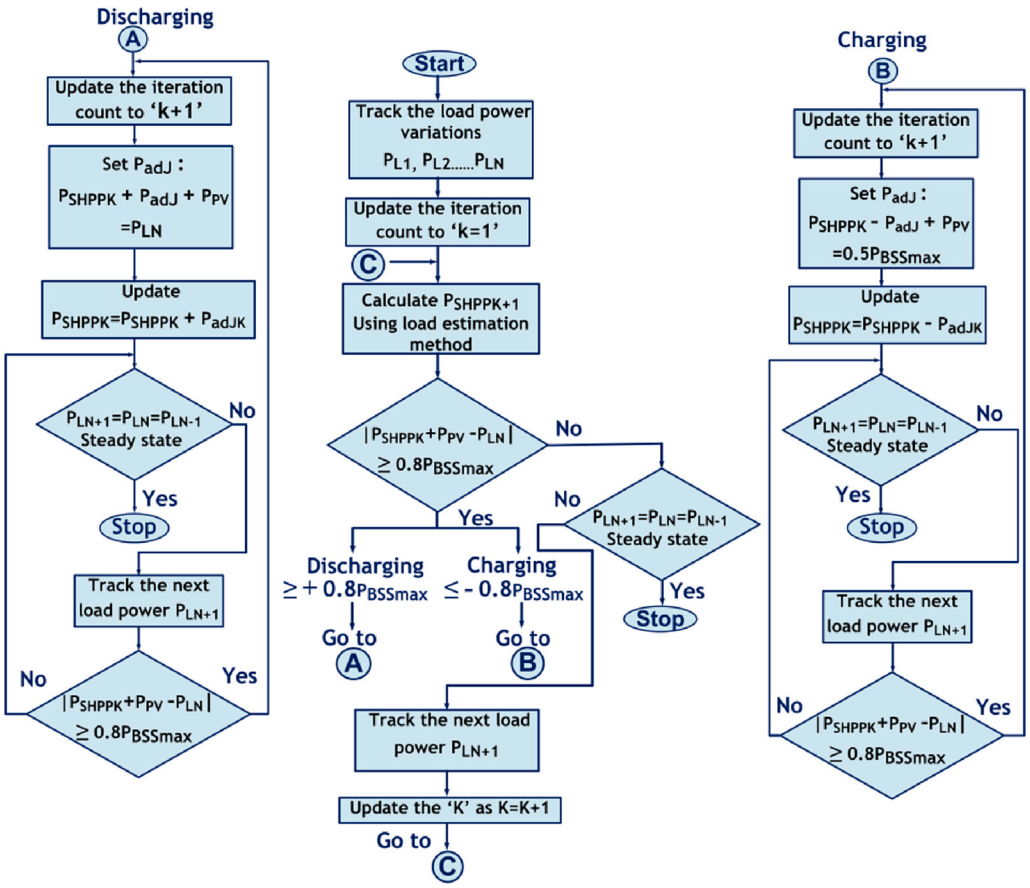

Fig. 11. Control algorithm of proposed AEMS.

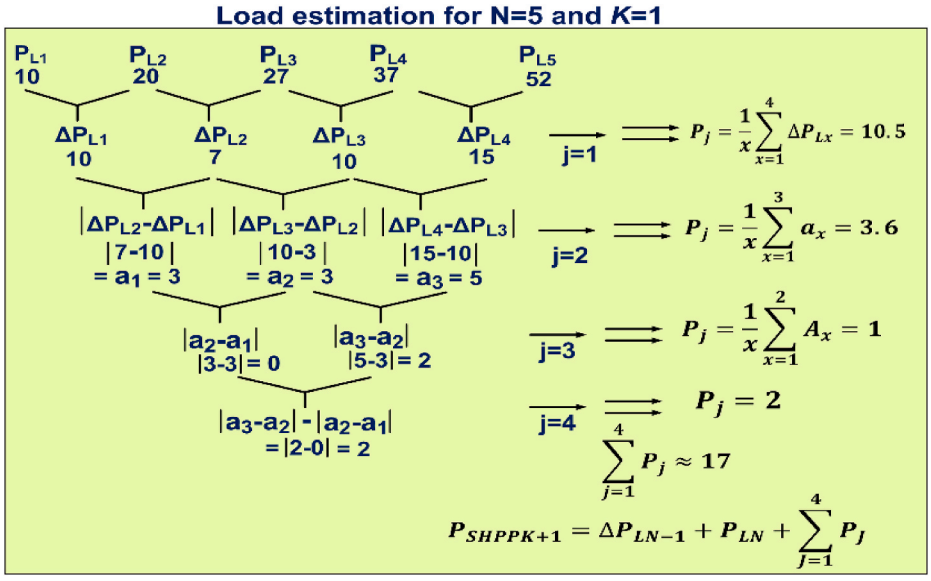

Fig. 12. Load power estimation to generate $P_{SHPPK+1}$ for $K = 1$.

shown in Fig. 11. This improves the optimal utilization of SHPP with reduced stress levels of BSS. Therefore, after the mismatch, K is not going to be updated for every 10s rather it gets updated after BSS has reached 80% of $|P_{BSSmax}|$ as shown in Fig. 11.

The updated output power of SHPP set by AEM for succeeding iteration count with reference to Eq. (34) & Eq. (35) are given as follows

$$P_{SHPPK} = P_{SHPPK} + P_{adJ} \tag{37}$$

$$P_{SHPPK} = P_{SHPPK} - P_{adJ} \tag{38}$$

If the load power dynamics results in $P_{LN+1} = P_{LN} = P_{LN-1}$ then AEM understands that load power dynamics have reached steady state. After steady state, AEM stops tracking the load power dynamics and locks the

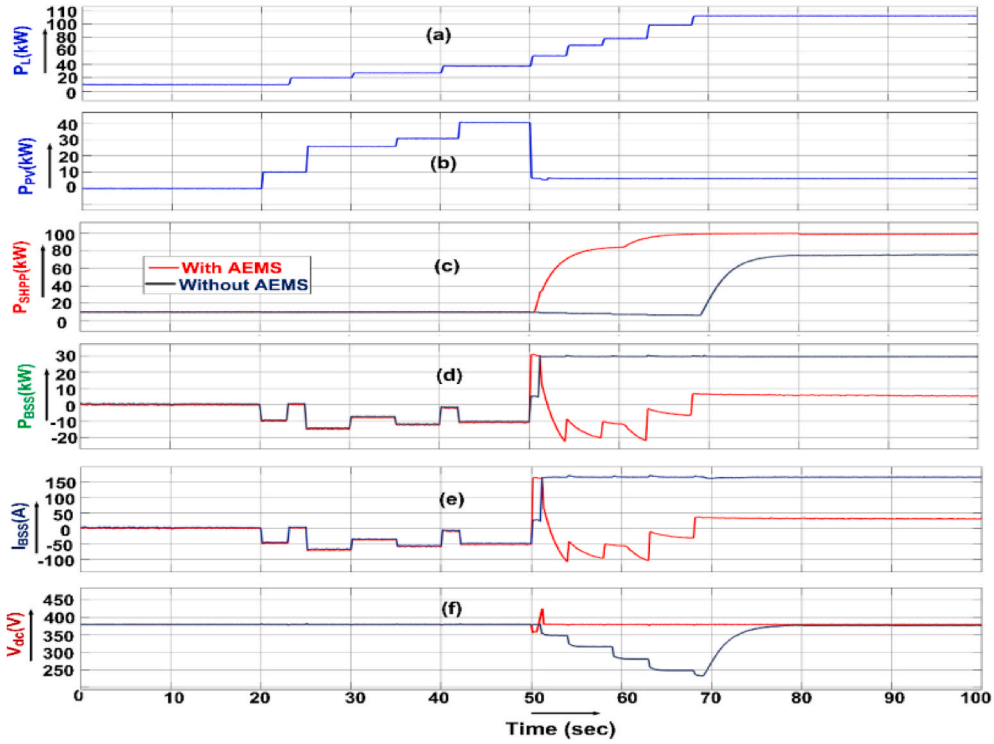

Fig. 13. (a) Load power dynamics for Case 1, (b) Solar PV power, (c) Output power of SHPP, (d) Output power of BSS, (e) Input current of BSS, (f) Voltage at the DC bus of MG.

Table 3
Power constraint of each source in the considered MG for comparison.

SHPP	Maximum output power of SHPP = 100 kW
Battery storage system	Maximum output power of BSS = 30 kW Maximum BSS current = 164A Capacity = 54Ahr C-rating of BSS = 3C
Fall in solar PV power output due to bad weather condition	14% of its maximum power (40 kW) = 5.6 kW

P_{SHPPK} as shown in Fig. 11. P_{LN+1} in Figs. 10 and 11 signifies the next load power change after P_{LN}. Therefore, using the control algorithm given in Fig. 11, the proposed AEMS maintains the power balance in the grid and attains sustainable voltage control of considered DC MG without exceeding the P_{BSSmax} of BSS.

4. Simulation results

This section is going to discuss the results associated with and without proposed AEMS against the following test load cases.

Case 1. Load power dynamics about the peak load condition: P_{BSS} is within 80% of P_{BSSmax}

Case 2. Sudden fall in load power demand during non-peak load condition: $P_{BSS} \geq$80% of $|P_{BSSmax}|$ in the charging mode

Case 3. Sudden rise in load power demand during the peak load condition: $P_{BSS} \geq$80% of $|P_{BSSmax}|$ in the discharging mode

The obtained MATLAB/Simulink results of AEMS for the aforementioned test load cases are presented in the following section.

4.1. *Case 1 with AEMS*

The load power dynamics during the peak load condition are shown in Fig. 13(a). The peak load for the considered DC MG is 110 kW. In Fig. 13(a), the load is varying at the rate of [10 20 27 37 52 67 77 97 110] kW for t = [0 23 30 40 50 54 58 63 68] s.

In Fig. 13(b), the abnormal situation of fall in solar PV power output to 5 kW (P_{PV} <6 kW) is occurred at t = 50s. As per the load estimation method shown in Fig. 12, at t = 50.5s, iteration count K is set to '1'. The delay of 0.5s accounts for the sensor time constant.

The step by step load power estimation procedure for '$K = 1$'is shown in Fig. 12. From Fig. 12, the estimated load power $P_{SHPPK+1}$ based on the following load dynamics (ΔP_{L1} = 10kW, ΔP_{L2} = 7kW, ΔP_{L3} = 10kW, P_{L4} = 37kW, P_{L5} = 52kW) from t = 23s–50s is given as $P_{SHPPK+1}$ = 84 kW. With reference to P_{SHGK+1} set by the AEMS, SHPP has delivered 84 kW to the load with a response time of 8.5 s as shown in Fig. 13(c). Consequently, based on the load dynamics for $K = 2$ the estimated load powerP_{SHGK+1} set by AEM is 110 kW. Since, the maximum power output of SHPP is 100 kW it has delivered 100 kW to the load with a response time of 8.5s as show in Fig. 13(c). At t = 68s, the power balancing equation with P_{L9} = 110 kW & $P_{SHPPK+1}$ = 100 kW is give as follows

$$P_{PV} + P_{SHPPK+1} - P_{L9} = +P_{BSS} = -5kW \tag{39}$$

Therefore, P_{BSS} = 5 kW balances the uncompensated load power of SHPP and maintains the constant V_{dc} according to Eq. (23). Since, P_{BSS} has not exceeded 80% of $|P_{BSSmax}|$ against the considered test load case, AEC has no role to play. As a result of power balance throughout the load power dynamics, a sustainable voltage of V_{dc} = 380V is maintained in this case as shown in Fig. 13(f).

4.1.1. *Case 1 without AEMS*

The active power flow control of BSS proposed in (Kewat and Singh, 2019), power management strategies adopted in (Kewat et al., 2018) and (Sharma et al., 2019) have commonly operated the BSS to compensate the load power dynamics during sudden fall in solar PV

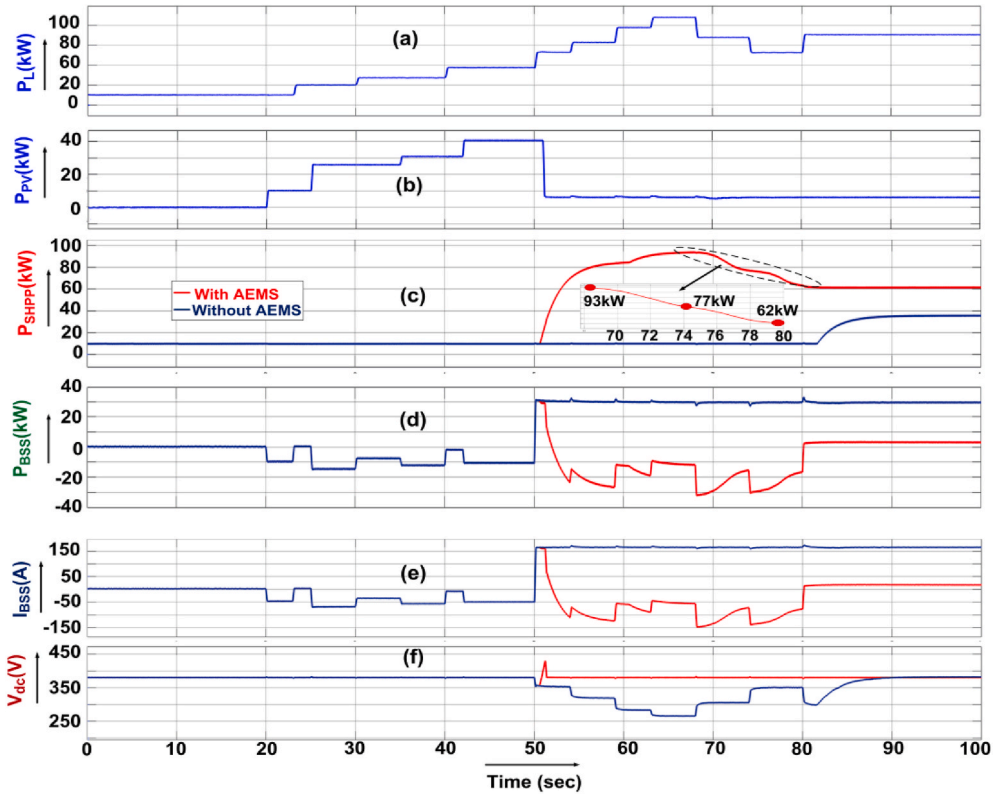

Fig. 14. (a) Load power dynamics for Case 2 (b) Solar PV power (c) Output power of SHPP (d) Output power of BSS (e) Input current of BSS (f) Voltage at the DC bus of MG.

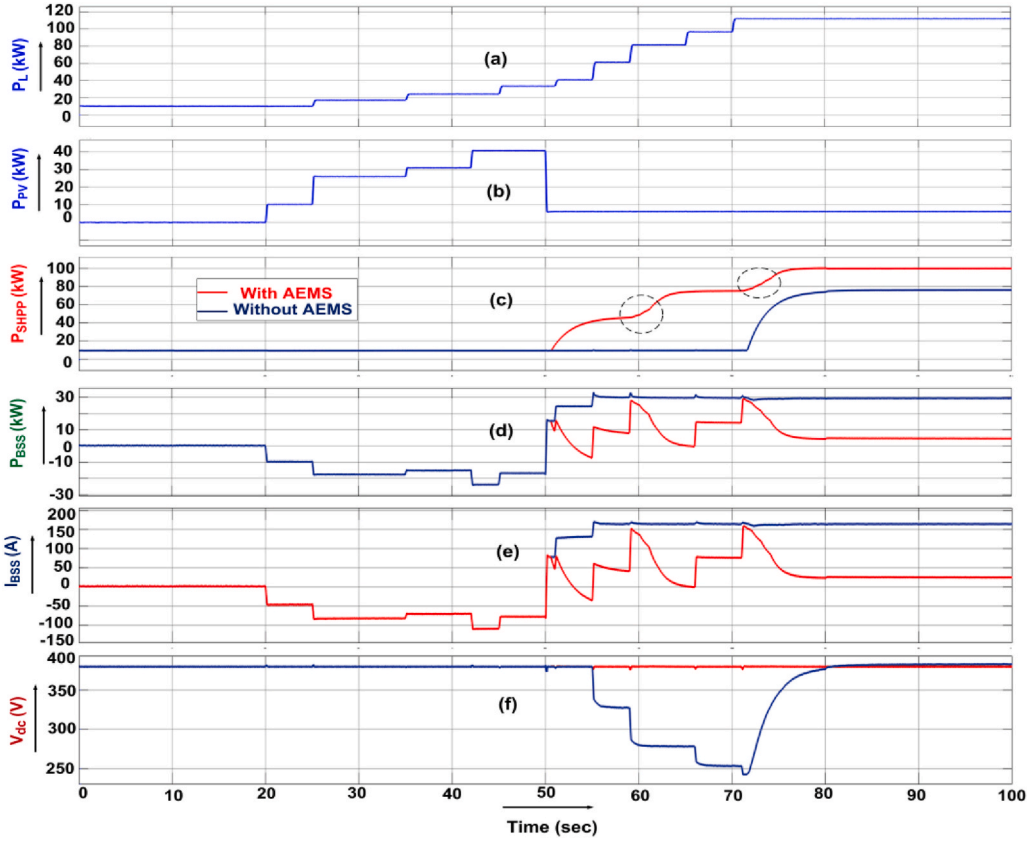

Fig. 15. (a) Load power dynamics for Case 3 (b) Solar PV power (c) Output power of SHPP (d) Output power of BSS (e) Input current of BSS (f) Voltage at the DC bus of MG.

Fig. 16. Set up for validating the proposed AEMS in the OPAL-RT RT-LAB.

power output. But, due to slow response time of SHPP and C-rate limitation of BSS, with reference to the aforementioned control strategies, SHPP is going to compensate the untracked load dynamics of hybrid MG once they have settle down. In this work, the power management strategies adopted in (Kewat and Singh, 2019; Kewat et al., 2018; Sharma et al., 2019) are referred as without CEMS, and the same is reported in Table 3.

The simultaneous fall in solar PV power to 5 kW at t = 50s and change in load power from 37 kW to 52 kW has led the output power of BSS shown in Fig. 13(d) reach its maximum power P_{BSSmax} = 30 kW corresponding to its 3C rate as given in Table 3. The maximum discharging current from BSS proportional to P_{BSSmax} is shown in Fig. 13(e) (navy blue).

In Fig. 13(f), at t = 50.2s, the imbalanced power of 7 kW between the load power demand (52 kW) and the total generation from BSS, solar PV, SHPP (P_{BSSmax}+P_{PV}+P_{SHPP} = 45 kW) made the voltage at the DC bus(V_{dc}) of MG fall from 380V to 350V as per the equation Eq. (23). Consequently, in Fig. 13(f), it can be observed that at t = 54s, 59s, 63s, 68s the uncompensated load of 67kW–44kW = 23 kW, 77kW–43kW = 34 kW, 97 kW–42.5 kW = 54.5 kW, 110 kW–41.2 kW = 67.8 kW has led the V_{dc} further fall to 318V, 282V, 250V, 235 respectively.

In Fig. 13(a) it is can be observed that the load power dynamics have settle down after t = 68s. As per the control strategies without AEMS, SHPP compensates the steady state load using the following equation

$$P_{SHGPP}(t) = (P_{SHG0} + P_{PV} + |P_{BSS}|) - P_{L9} = 75kW \tag{40}$$

Therefore, SHPP has delivered 75 kW to the load as shown in Fig. 14 (c) (blue color). As there is a load-generation balance in the grid (P_{BSSmax}+P_{PV}+P_{SHPP} = 110 kW), V_{dc} as per Eq. (23) get back to its nominal value (380V) after t = 78s as shown in Fig. 13(f) (navy blue).

4.2. *Case 2 with AEMS*

The load power dynamics during non-peak load condition are shown in Fig. 14(a). It can be observed that in Fig. 16 (a), load is varying at the rate of [10 20 27 37 52 62 77 87 67 52 70] kW for t = [0 23 30 40 50 54 59 63 68 74 80] s. As soon as the abnormality occurs after t = 50s, then as per the load estimation method shown in Fig. 10, $P_{SHPPK+1}$ set by AEM for K = 1 is given as 84 kW.

Corresponding to $P_{SHPPK+1}$ set by AEM, SHPP has delivered 84 kW to the load from t = 50.5s with a response time of 8.5s shown in Fig. 14(c).

Consequently, for the next iteration i.e. K = 2, $P_{SHPPK+1}$ set by the load estimator is 123.5 kW, but the maximum power can be delivered by the SHPP is 100 kW. Therefore, SHPP has set to deliver 100 kW from t = 60.5s. But, due to the mismatch between estimated load and actual load (P_{L9} = 67 kW) at t = 68s the battery has reached 80% $|P_{BSSmax}|$ in the charging mode as shown in Fig. 14(d). Then AEM has let the AEC to adjust the output power of SHPP in such a way that

$$P_{SHPPK}(=93kW) + P_{PV} - (P_{adJ} = 16kW) - (P_{L9} = 67kW) = 50\%of\ |P_{BSSmax}| \tag{41}$$

$$P_{adJK} = \frac{1}{(1 + sT_{SPMS})}(P_{adJ1} \times 4 + P_{adJ2} \times 3 + P_{adJ3} \times 2 + P_{adJ4} \times 1) \tag{42}$$

where, $P_{adJ1}, P_{adJ2}, P_{adJ3}, P_{adJ4}$ = $4kW, 8kW, 12kW, 16kW$

In the zoomed view of Fig. 14(c) it is shown that, after AEC's power adjustment of −15kW, P_{SHPPK} has become 93kW–15kW = 78 kW at t = 73.5s. In response to thisP_{BSS} has reached 15 kW (=50% of P_{BSSmax}) at t = 73.5s as shown in Fig. 14(d).

In Fig. 14(a), the sudden fall in load power from 68 kW to 52 kW at t = 74s leads the BSS again hit 80% of $|P_{BSSmax}|$ in the charging mode shown in Fig. 14(d). Therefore, as per the control algorithm given in Fig. 11, again AEC has set P_{adJK} = − 15 kW in such a way that P_{SHPPK}(= 77 kW) + P_{PV} − (P_{adJ} = 15 kW) − (P_{L10} = 52 kW) = 50% of $|P_{BSSmax}|$. The load power P_{L11} = 70 kW at t = 80s is compensated by the BSS in such a way that P_{SHPPK}(= 62 kW) + P_{PV}(=5 kW) + P_{BSS}(=3 kW) = P_{L11}(=70 kW).

Due to tight power balance throughout the load power fluctuations, V_{dc} shown in Fig. 14(e) has remained constant. By keeping in mind the settling time of V_{dc} without AEMS, T_{SS} in this case is chosen as 90 s.

4.2.1. *Case 2 without AEMS*

The load power dynamics shown in Fig. 14(a) without AEMS has resulted in unbalanced power flow of [7 17 32 42 22 7 25] kW for [50–54 54-59 63–68 68-74 74–80] s. This unbalanced power flow has led the V_{dc} fall from 380V to [355 320 284 265 305 350 300] V as shown in Fig. 14(f) (navy blue). Since, the load power dynamics have reached steady state after t = 80s, with reference to control strategies given in without AEMS, SHPP has delivered 35 kW to the load with a response time of 8.5s. This is shown in Fig. 14(c) (navy blue). Due to the load-generation balance, V_{dc} has recovered from 300V at t = 80s to 380V at t = 90s as shown in Fig. 14(f) (navy blue).

4.3. *Case 3 with AEMS*

The load power variations in this case are shown in Fig. 15(a). In Fig. 15(a), the load is varying at the rate of [10 17 24 31 41 60 80 95 110] kW for t = [0 25 35 45 51 55 59 66 71] s. With reference to the estimated load power set by the AEM for K = 1, SHPP has dispatched 45.5 kW to the load with a settling time of 8.5s as shown in Fig. 15(c). But, the sudden change in load from 60 kW to 80 kW at t = 59s has led to mismatched load power of 28 kW(P_{SHPPK}(= 45.5kW) + P_{SHPPK}(= 5kW) − P_{L7}(= 80kW) = 29.5kW). Therefore, battery has compensated this mismatched load power due to the exceeded limit i.e. > 80% $|P_{BSSmax}|$. Since P_{BSS} > 80% $|P_{BSSmax}|$, AEC has adjusted the output power of SHPP in such a way that

Fig. 17. OPAL-RT results for Case 1. (a) Voltage at the DC bus of MG, (b) Load power dynamics, (c) Output power of BSS, (d) Output power of SHPP, (e) Input current of BSS, (f) Solar PV power.

$$P_{SHPPK}(45.5kW) + P_{PV}(5kW) + P_{adJ}(29.5kW) = P_{L7}(80kW) \quad (43)$$

Consequently, the mismatch between the load power of 110 kW at t = 71s and P_{SHPP} = 75 kW has led the battery again exceed its limit i.e. 80% $|P_{BSSmax}|$ in the discharging mode. Therefore, to compensate this load, with reference to the AEC's adjusted output power, SHPP has delivered 100 kW to the load with a proportional increase in P_{SHPP} from 75 kW at t = 71s to 100 kW at t = 76.5s. This is represented in Fig. 15(c) with a dotted circle. Hence, due to the tight power balance against the load dynamics considered in this case, V_{dc} has remained constant. The same is shown in Fig. 15(f).

4.3.1. *Case 3 without AEMS*

Since, load power dynamics (Fig. 15(a))in Case 3 have settle down after t = 71s, SHPP has delivered 75 kW to the load with a response time of 8.5s as explained in Case 2 without AEMS and the same is shown in Fig. 15(c). Due to the power balance between the generation and load as given below

$$P_{SHPPK}(75kW) + P_{PV}(5kW) + P_{BSS}(30kW) = P_{L7}(110kW) \quad (44)$$

The voltage at the DC bus of MG with reference to Eq. (23) has recovered to its nominal value at t = 80s. The recovery of V_{dc} from t = 71.5s–80s can be seen in Fig. 15(f).

5. Real time validation of proposed AEMS in OPAL-RT

In this section, the real time compatibility of MATLAB/Simulink model of AEMS is tested. The objective of real time simulator is that it can produce the results of test system under actual electrical conditions just like real time hardware (Sorto-Ventura et al., 2020). In this work, the MATLAB/Simulink model of AEMS is tested in OPAL-RT real time simulator (OP4510). The OP4510 shown in Fig. 16 comprises 4 core processor, Kintex-7 FPGA (field programmable gate array), 32 Digital I/O channels and 16 Analog I/O channels for communicating with the real time environment. The Kintex-7 FPGA used in OP4510 is best suitable for high switching frequency applications such as PWM generating circuits of power electronic converters. The detailed architecture of RT-LAB is given in (Singh et al., 2014).

The test bench for validating the Simulink model of AEMS is shown in Fig. 16. To produce the real time results, OP4510 uses RT-Lab for interfacing the Simulink model loaded in the host PC (shown in Fig. 16) with the real time simulator. The RT-Lab makes the communication between the MATLAB/Simulink model of AEMS developed in the host PC and the real time simulator (shown in Fig. 16) by compiling the Simulink model to executable code that can run on real time simulator. Then, the central processing unit of OP4510 runs this code and generates real time results.

The real time results from OP4510 are captured in the digital oscilloscope as shown in Fig. 16. In this work, to ensure the compatibility between designed MATLAB/Simulink model and the real time simulator, the sampling time of it chosen as 10μs. The obtained real time simulation results of proposed AEMS for various test load cases are discussed below.

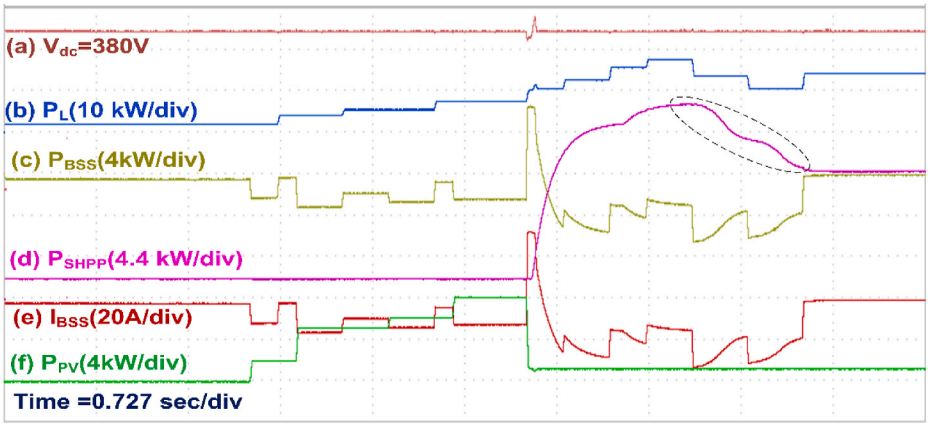

Fig. 18. OPAL-RT results for Case 2. (a) Voltage at the DC bus of MG, (b) Load power dynamics, (c) Output power of BSS, (d) Output power of SHPP, (e) Input current of BSS, (f) Solar PV power.

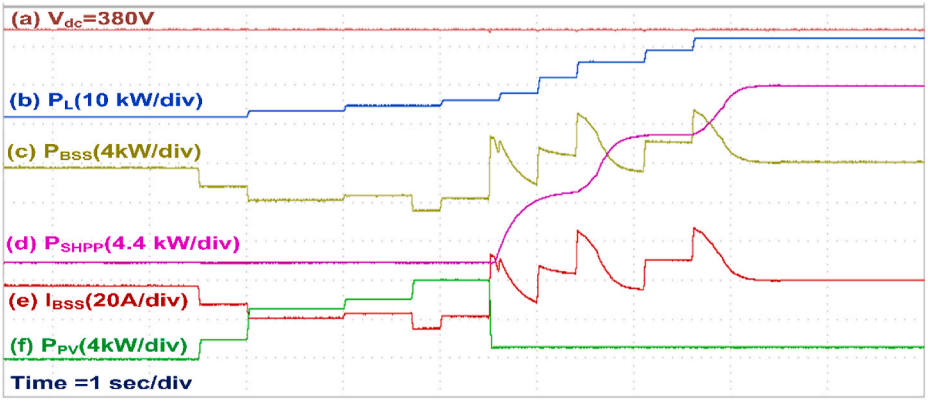

Fig. 19. OPAL-RT results for Case 3. (a) Voltage at the DC bus of MG, (b) Load power dynamics, (c) Output power of BSS, (d) Output power of SHPP, (e) Input current of BSS, (f) Solar PV power.

5.1. Real time validation of AEMS for Case 1

The load power dynamics for Case 1 in the OPAL-RT real time simulator are shown in Fig. 17(b). To maintain the power flow control of DC MG during the abnormal situation as explained in section 4.1, AEMS has generated a reference power of 84 kW and 100 kW for $K = 1$ and $K = 2$ respectively. Therefore with reference to $P_{SHPPK+1}$ set by the AEMS for $K = 1$ & $K = 2$, SHPP has delivered 84 kW and 100 kW to load with a response time of 8.5s as shown in Fig. 17(d). With a keen observation it is inferred that the dynamic change in the output power of SHPP in real time simulator (ref. Fig. 17(d)) is same as the MATLAB/Simulink result shown in Fig. 15(c).

The untracked load power of SHPP compensated by BSS during $K = 1$ and $K = 2$ is shown in Fig. 17(c). Since, $P_{BSS} < 80\%|P_{BSSmax}|$ throughout load power dynamics, role of AEC is absent in this case. The same is justified with the current delivered by the BSS shown in Fig. 17(e). The tight balance ensured by AEMS with active participation of SHPP and BSS during the load power dynamics has led the V_{dc} remained constant as shown in Fig. 17(a). It can be observed that, the V_{dc} in Fig. 17(a) is just a replica of Simulink result presented in Fig. 15(f). Hence, OPAL-RT results presented in this section are in agreement with Simulink results presented in section 4.1.

Table 4
Relative comparison between with and without AEMS.

Test case		%Voltage sustainability	% U.F of SHPP	I_{BSSavg}(A)	%Discharging current stress levels of BSS
Case 1	Sharma et al. (2019)	77.3	23.29	161.38	98.40
	"Standard for the Sp (2018)	77.3	23.29	161.38	98.40
	Li et al. (2020)	77.3	23.29	161.38	98.40
	With AEMS	100	78.56	0.39	0.23
Case 2	Sharma et al. (2019)	62.968	10.614	164	100
	"Standard for the Sp (2018)	62.968	10.614	164	100
	Li et al. (2020)	62.968	10.614	164	100
	With AEMS	100	65.038	−34.844	0
Case 3	Sharma et al. (2019)	80.30	17.84	154.41	94
	"Standard for the Sp (2018)	80.30	17.84	154.41	94
	Li et al. (2020)	80.30	17.84	154.41	94
	With AEMS	100	67.09	42.6125	25.9

5.2. Real time validation of AEMS for Case 2

The load power dynamics for Case 2 are shown in Fig. 18(b). In this case the mismatch between estimated load $P_{SHPPK+1} = 100$ kW and actual load $P_{L9} = 67$ kW at t = 68s has lead the BSS reach 80% of $|P_{BSSmax}|$ in the charging mode as shown in Fig. 18(c).

Therefore, with reference to the AEMS control algorithm, AEC has adjusted the output power of SHPP in such a way that $P_{BSS} = 50\%$ of $|P_{BSSmax}|$. This is shown in Fig. 18(c). From the OPAL-RT results presented in Fig. 18, it is inferred that the dynamics of P_{SHPP}, P_{BSS}, I_{BSS} and V_{dc} in real time simulation and MATLAB/Simulink environment are in agreement. Therefore, the MATLAB/Simulink results presented in section 4.2 (with AEMS) are validated in the real time simulator.

5.3. Real time validation of AEMS for Case 3

The real time simulation results for Case 3 are shown in Fig. 19. In this case, the mismatched load power lead the BSS reach 80% of $|P_{BSSmax}|$ in the discharging mode at t = 59s and 71s is shown in Fig. 19(c). The proposed control algorithm of AEMS (ref. Fig. 11) let AEC adjust the output power of SHPP in such a way that the load power demand at t = 65s and t = 76s gets compensated. This is justified with P_{BSS} becoming 0 at 65s and 10 kW after t = 76s in Fig. 19(c). The dynamics of P_{SHPP}, P_{BSS},

Table 5
Relative analysis of % sizing of battery storage.

References	Total generation capacity of Hydro, PV and Battery storage system	Maximum output power of battery storage system	% Sizing of battery storage system	% Improvement With AEMS
Sharma et al. (2019)	3.7 kW Hydro, 8.4 kW from PV 50Ah, 1C, 240V BSS	11.4 kW	94.21	73.21
"Standard for the Sp (2018)	3.7 kW Hydro, 2.48 kW from PV 14Ah, 1C, 240V BSS	3.192 kW	51.65	30.65
Li et al. (2020)	3.7 kW Hydro,1.585 kW from PV 35Ah, 1C, 253V BSS	8.412 kW	159.16	138.16
Proposed AEMS	100 kW Hydro, 40kw solar 54Ah, 3C, 195V BSS	30 kW	21	

I_{BSS} and V_{dc} observed in the real time simulator are same as the MATLAB/Simulink results presented in section 4.3 (with AEMS).

6. Comparative analysis between with and without applying proposed AEMS

To evaluate the superiority of proposed AEMS over active power flow control of BSS (Sharma et al., 2019), power management strategies adopted in ("Standard for the Sp, 2018) and (Li et al., 2020), the following performance factors are considered in this work.

$$\%\ \text{Voltage sustainability} = \frac{\frac{1}{T_{ss}-50}\sum_{t=50}^{t=T_{ss}}(V_{dc}\times t)}{V_{dcrf}}\times 100 \quad (45)$$

Voltage sustainability indicates how optimally the power flow is managed in the considered DC MG especially when it is operating under the abnormal situation as reported in this work.

$$\%\,\text{Utilization factor (U.F.) of SHPP} = \frac{\frac{1}{T_{ss}-50}\sum_{t=50}^{t=T_{ss}}(P_{SHPP}\times t)}{\text{Maximum output power of SHPP}}\times 100 \quad (46)$$

Utilization factor signifies the active contribution of main dispatchable power source during abnormal situation. High utilization factor of SHPP improves the reliability, voltage sustainability of MG. Moreover, it reduces current stress levels of BSS as well.

$$\text{Average current of BSS } (I_{BSSavg}) = \frac{1}{T_{ss}-50}\sum_{t=50}^{t=T_{ss}}(I_{BSS}\times t) \quad (47)$$

$$\%\ \text{Discharging current stress levels of BSS} = \frac{I_{BSSavg}(A)}{\text{Maximum discharging current corresponding to 3C rate of BSS}}\times 100 \quad (48)$$

Average current of BSS is used to calculate the current stress levels of it. Moreover, I_{BSSavg} has direct relation with battery life. Closer the I_{BSSavg} to I_{BSSmax} lesser will be the battery life.

Discharging current stress level indicates how closely the battery is operating around its maximum current limit (I_{BSSmax}) corresponding to 3C rate in the discharging mode.

In this work, the performance factors are calculated from the obtained results of $V_{dc}, P_{SHPP}, I_{BSS}$ in the respective cases.

The calculated values of performance factors for Case 1 are given in section 6.1. Similarly, the calculated values of performance factors for Case 2 and Case 3 are given in Table 4. From the comparative results presented in Table 4, it is inferred that compared to without AEMS, voltage sustainability of hybrid DC MG with AEMS is enhanced by 22.7%, 37% and 19.7% for Case 1, Case 2 and Case 3 respectively.

The utilization factor with AEMS is improved by 55.275%, 54.424% and 49.66% compared to without AEMS for Case 1, Case 2 and Case 3 respectively. Due to improved utilization of SHPP, the discharging current stress levels of BSS has been reduced by 98.39%, 100% and 72% compared to without AEMS for Case 1, Case 2 and Case 3 respectively.

Furthermore, from Table 5 it is evident that utmost utilization of SHPP with the proposed AEMS has reduced the % sizing of BSS by 70%, 68% and 50% compared to the % sizing of BSS used in (Sharma et al., 2019), ("Standard for the Sp, 2018) and (Li et al., 2020) respectively. In this work, % sizing of BSS is chosen based on the maximum output power delivered by it for 1 h with the presence of the total distributed capacity. Moreover, maximum output power of BSS is calculated with 5% drop in the terminal voltage of BSS. The % sizing of BSS is calculated based on the following formulae

$$\%\ \text{Sizing of battery storage} = \frac{\text{Maximum output power of battery storage system(kW)}}{\text{Total generation from hydro and PV (kW)}}\times 100 \quad (49)$$

$$\text{Maximum output power of battery storage} = \frac{(Capacity\ of\ BSS)}{1\ hour} \times \text{terminal voltage of BSS} \quad (50)$$

The quantitative calculations regarding the % sizing of BSS are given in section 6.1.1. The obtained results are reported in Table 5.

6.1. Calculation of performance factors for Case 1

% Voltage sustainability:
With AEMS.
For Case 1 with. $T_{ss} = 80s$
Without AEMS

$$\frac{\left(\frac{1}{30}\sum_{t=50}^{t=80}(V_{dc}\times t)\right)}{V_{dcrf}}\times 100 = \frac{\frac{8816.6}{30}}{380} = 77.33\%\ \text{With AEMS}$$

$$\frac{\left(\frac{1}{30}\sum_{t=50}^{t=80}(V_{dc}\times t)\right)}{V_{dcrf}}\times 100 = \frac{380}{380} = 100\%$$

% Utilization factor of SHPP:
Without AEMS

$$\frac{\frac{1}{30}\left(\sum_{t=50}^{80}(P_{SHPP}\times t)\right)}{100}\times 100 = \frac{\frac{698.85}{30}}{100}\times 100 = 23.29\%$$

With AEMS

$$\frac{\frac{1}{30}\left(\sum_{t=50}^{80}(P_{SHPP}\times t)\right)}{100}\times 100 = \frac{\frac{2357}{30}}{100}\times 100 = 78.56\%$$

Average current of BSS:
Without AEMS

$$= \frac{1}{30}\sum_{t=50}^{t=80}(I_{BSS}\times t) = \frac{4841.4}{30} = 161.38A$$

With AEMS.

$$= \frac{1}{30}\sum_{t=50}^{t=80}(I_{BSS}\times t) = \frac{24.275}{30} = 0.89A$$

Discharging current stress levels of BSS:
Without AEMS

$$= \frac{161.38}{164}\times 100 = 98.4\%$$

With AEMS

$$= \frac{0.39}{164}\times 100 = 0.23\%$$

6.1.1. Calculation % sizing of battery storage system

Maximum output power of BSS:

$= \frac{(50\ Ah)}{1\ hour} \times 228 = 11.4kW$ For (Sharma et al., 2019).
$= \frac{(14Ah)}{1\ hour} \times 228 = 6.18kW$ For ("Standard for the Sp, 2018).
$= \frac{(35Ah)}{1\ hour} \times 223 = 7.81kW$ For (Li et al., 2020).
$= \frac{(61\ Ah)}{1\ hour} \times 185.25 = 30kW$ For proposed AEMS.
Sizing of BSS:
$= \frac{(11.4)}{12.1} \times 100 = 94.21$ For (Sharma et al., 2019).
$= \frac{(3.192)}{6.18} \times 100 = 51.65$ For ("Standard for the Sp, 2018).
$= \frac{(8.412)}{5.285} \times 100 = 159.16$For (Li et al., 2020).
$= \frac{(30)}{140} \times 100 = 21$ For proposed AEMS.

7. Conclusion

The proposed AEMS in this work has attained the sustainable voltage control of clean energy sources (solar PV & SHPP) interfaced hybrid DC MG against the sudden fall in solar PV power output during the load dynamics. The novel aspect of the proposed smart AEMS is that despite the multiple constraints such as sudden rise/fall in load dynamics during peak/non-peak load condition, slow response time of SHPP and limited storage capacity of BSS, it has realized the sustainable voltage control of MG through a load estimation algorithm and adjustable energy controller mechanism. The iterative basis load estimation algorithm of proposed AEMS has led the SHPP compensate the load power dynamics despite its slow response time. The adjustable energy controller of AEMS has led the BSS compensate the mismatched load power without exceeding the maximum power limit corresponding to its C-rate either in charging or discharging mode. Based on the results obtained for various test load cases, a comparative analysis between AEMS and existed control strategies in the literature are carried out. From the comparative analysis it is evident that proposed smart AEMS has achieved 22.7% enhanced voltage sustainability and 53.27% improved utilization of hydro generation with 98.39% reduced discharging current stress level of battery storage system. Hence, the proposed smart AEMS has achieved the voltage sustainability of DC MG with reduced current stress levels of BSS and optimal utilization of clean energy sources. The extended version of proposed AEMS can be configured to achieve the optimal utilization, environmental feasibility of cleaner energy sources interfaced hybrid MG against the solar PV dynamics, small scale industrial and EV load dynamics.

CRediT authorship contribution statement

K. Raghavendra Naik: Methodology, Software, Validation, Formal analysis, Investigation, Visualization, Writing – original draft. **Bhooshan Rajpathak:** Supervision, Resources, Methodology, Conceptualization, Investigation, Writing – review & editing. **Arghya Mitra:** Supervision, Resources, Methodology, Conceptualization, Investigation, Writing – review & editing. **Mohan Lal Kolhe:** Methodology, Conceptualization, Visualization, Formal analysis, Investigation, Writing – review & editing, Supervision.

Declaration of competing interest

The authors declare that they have no known competing financial interests or personal relationships that could have appeared to influence the work reported in this paper.

Appendix I

PMSG: 400V, Maximum $P_{SHPP} = 100$ kW, $\omega_{eg} = 104.71$ rad/s, $J = 81.416$ kg-m^2, $R_s = 0.05\Omega$, $L_s = 0.52$ mH.
Turbine: $H_t = 4.5$m, Length of draft tube (L_t) = 17.6m, efficiency $\eta = 75\%$, Density of water $\rho = 1000$ kg/m^3
Rated flow rate $Q_t = 3m^3/sec$, Rated velocity $U_t = 2.5\ m/sec$, $T_{Wt} = 1\ sec$, Turbine gain. $A_{tg} = 1.136$
Solar PV array: $Y_{ref} = 1000$ W/m^2, Line inductance of boost converter. $L_{PV} = 0.352mH$

References

IEEE standard for the specification of microgrid controllers. In: IEEE Std 2030.7-2017, 23 April 2018, pp. 1–43. https://doi.org/10.1109/IEEESTD.2018.8295083.

Al-Shetwi, A.Q., Hannan, M.A., Jern, K.P., Mansur, M., Mahlia, T.M.I., Dec. 2019. Grid-connected renewable energy sources: review of the recent integration requirements and control methods. J. Clean. Prod. 253, 1–37.

Borkowski, D., Dec. 2018. Analytical model of small hydropower plant working at variable speed. IEEE Trans. Energy Convers. 33 (4), 1886–1894.

Central Statistics Office Energy Statistics 2019, 2019. Govt. India 2019. Central Statistics Office Energy Statistics 2019, Govt. India. Available. http://www.mospi.gov.in/sites/default/files/publication_reports/Energy %20Statistics%202019-finall.pdf.

Chandran, V.P., Murshid, S., Singh, B., 18 3 2020. Novel band pass filter-based control strategy for control of a hydro-PV-BES supported isolated MG. IET Power Electron. 13 (4), 636–648.

Comino, L. Dominici, Ambrogio, F., Rosso, M., March. 2020. Mini-hydro power plant for the improvement of urban water-energy nexus toward sustainability - a case study. J. Clean. Prod. 249, 1–21.

Cortés, P., Auladell-León, P., Muñuzuri, J., Onieva, L., April, 2020. Near-optimal operation of the distributed energy resources in a smart microgrid district. J. Clean. Prod. 252, 1–22.

da Silva, I.R.S., Rabelo, R. de A.L., Rodrigues, J.J.P.C., Solic, P., Carvalho, A., Jan. 2020. A preference-based demand response mechanism for energy management in a microgrid. J. Clean. Prod. 225, 1–14.

Deshmukh, R.R., Ballal, M.S., Suryawanshi, H.M., Nov.-Dec. 2020. A fuzzy logic based supervisory control for power management in multibus DC microgrid. IEEE Trans. Ind. Appl. 56 (6), 6174–6185.

Dikshit, K.R., Dikshi, J.K., 2014. Introduction. In: North-east India: Land, People and Economy. Advances in Asian Human-Environmental Research. Springer, Dordrecht.

Executive Summary on Power Sector for September 2018, 2018. Available. https://www.cea.nic.in/reports/monthly/executive.summary/2018/exe_summary-09.pdf.

Executive Summary on Power Sector for September 2019, 2019. Available. https://cea.nic.in/reports./monthly/executive.summary/2019/exe_summary-09.pdf.

Executive Summary on Power Sector for September 2020, 2020. Available. https://cea.nic.in/reports/monthly/executive.summary/2020/exe_summary-09.pdf.

Guan, Y., Vasquez, J.C., Guerrero, J.M., Wang, Y., Feng, W., Nov.-Dec. 2015. Frequency stability of hierarchically controlled hybrid photovoltaic-battery-hydropower microgrids. IEEE Trans. Ind. Appl. 51 (6), 4729–4742.

Kalita, P., Das, S., Das, D., Borgohain, P., Dewan, A., Banik, R.K., August, 2019. Feasibility study of installation of MW level grid connected solar photovoltaic power plant for northeastern region of India. In: Sādhanā, vol. 207.

Kalla, U.K., Singh, B., Murthy, S.S., Jain, C., Kant, K., Nov. 2018. Adaptive sliding mode control of standalone single-phase microgrid using hydro, wind, and solar PV array-based generation. IEEE Trans. Smart Grid 9 (6), 6806–6814.

Kesilmiş, Z., Karabacak, M.A., Aksoy, M., Sept. 2020. A novel MPPT method based on inflection voltages. J. Clean. Prod. 266, 1–11.

Kewat, S., Singh, B., 7 8 2019. Modified amplitude adaptive control algorithm for power quality improvement in multiple distributed generation system. IET Power Electron. 12 (9), 2321–2329.

Kewat, S., Singh, B., Hussain, I., 19 3 2018. Power management in PV-battery-hydro based standalone microgrid. IET Renew. Power Gener. 12 (4), 391–398.

Li, C., Jia, X., Zhou, Y., Li, X., March, 2020. A microgrids energy management model based on multi-agent system using adaptive weight and chaotic search particle swarm optimization considering demand response. J. Clean. Prod. 262, 1–15.

Li, Y., et al., Sept. 2019. Analysis and enhancement of PV efficiency with hybrid MSFLA–FLC MPPT method under different environmental conditions. J. Clean. Prod. 271, 1–21.

Ling, W., Zhou, Y., Wu, H., et al., 2019. A compensation power control strategy for DFIG and PMSG in a wind–PV–hydro hybrid system. Iran J. Sci. Technol. Trans. Electr. Eng. 43, 519–530.

Manandhar, U., et al., March 2019. Energy management and control for grid connected hybrid energy storage system under different operating modes. IEEE Trans. Smart Grid 10 (2), 1626–1636.

Microgrids, Smart, 2017. Re-visioning Smart Grid and Smart City Development in India, India Smart Grid Forum March. Available. https://indiasmartgrid.org/event2017/2.%20Larisa.%20Dobriansky.pdf.

Naik, K.R., Rajpathak, B., Mitra, A., Kolhe, M.L., 2021. Energy management technique assessment for achieving sustainable voltage during islanded operation of DC microgrid interfaced with hydro generator. In: Sustainable Energy Technologies and Assessments.

Olatunde, O., Yusri Hassan, M., Abdullah, M.P., Rahman, H.A., 2020a. Hybrid photovoltaic/small-hydropower microgrid in smart distribution network with grid isolated electric vehicle charging system. J. Energy Storage 31, 1–15.

Olatunde, O., Hassan, M.Y., Abdullah, M.P., Rahmann, H.A., July.2020. Hybrid photovoltaic/small-hydropower microgrid in smart distribution network with grid isolated electric vehicle charging system. J. Energy Storage 31, 1–15.

Padmanathan, K., et al., April, 2019. A sociocultural study on solar photovoltaic energy system in India: stratification and policy implication. J. Clean. Prod. 216, 1–46.

Reddy, K.M., Singh, B., Sept. 2018. Multi-objective control algorithm for small hydro and SPV generation based dual mode reconfigurable system. IEEE Trans. Smart Grid 9 (5), 4942–4952.

Sadanala, S. Pattnaik and V. P. Singh, "A novel switched capacitor based multilevel inverter with symmetrical and asymmetrical configurations," in Electr. Eng., doi: 10.1007/s00202-020-01172-7.

Sadanala, S. Pattnaik and V. P. Singh, "A flying capacitor based multilevel inverter architecture with symmetrical and asymmetrical configurations," in IEEE J. Emerg. Selected Topics Power Electr., doi: 10.1109/JESTPE.2020.3029681.

C. Sadanala, S. Pattnaik and V. P. Singh, "Fault tolerant architecture of an efficient five-level multilevel inverter with overload capability characteristics," in IET Power Electron., vol. 13, no. 2, pp. 368-376, 5 2 2020, doi: 10.1049/iet-pel.2019.0736.

Schoonenberg, W.C.H., Farid, A.M., Oct.2017. A dynamic model for the energy management of microgrid-enabled production systems. J. Clean. Prod. 164, 816–830.

Sharma, R., Kewat, S., Singh, B., Oct. 2019. Robust 3IMPL control algorithm for power management of SyRG/PV/BES-Based distributed islanded microgrid. IEEE Trans. Ind. Electron. 66 (10), 7765–7777.

Sharma, R., Kewat, S., Singh, B., May-June 2020. SyRG-PV-BES-based standalone microgrid using approximate multipliers based adaptive control algorithm. IEEE Trans. Ind. Appl. 56 (3), 2913–2924.

Shezan, S.A., Dec. 2020. Feasibility analysis of an islanded hybrid wind-diesel-battery microgrid with voltage and power response for offshore Islands. J. Clean. Prod. 288.

Singh, S.K., Padhy, B.P., Chakrabarti, S., Singh, S.N., Kolwalkar, A., Kelapure, S.M., 2014. Development of dynamic test cases in OPAL-RT real-time power system simulator. In: 2014 Eighteenth National Power Systems Conference. NPSC), Guwahati, pp. 1–6.

Singh, B., Sharma, R., Kewat, S., April 2021. Robust control strategies for SyRG-PV and wind-based islanded microgrid. IEEE Trans. Ind. Electron. 68 (4), 3137–3147.

Sorto-Ventura, K.-R., Abarzadeh, M., Al-Haddad, K., Dessaint, L.A., 2020. 23-level single DC source hybrid PUC (H-PUC) converter topology with reduced number of components: real-time implementation with model predictive control. IEEE Open J. Industr. Electr. Soc. 1, 127–137.

Ullah, S., Haida, A.M.A., Hoole, P., Zen, H., Ahfock, T., Nov.2020. The current state of Distributed Renewable Generation, challenges of interconnection and opportunities for energy conversion based DC microgrids. J. Clean. Prod. 273, 1–36.

Yi, Z., Dong, W., Etemadi, A.H., Nov. 2018. A unified control and power management scheme for PV-Battery-Based hybrid microgrids for both grid-connected and islanded modes. IEEE Trans. Smart Grid 9 (6), 5975–5985.

Yuan, W., Liu, Z., Su, C., Wang, X., Dec. 2020. Photovoltaic capacity optimization of small and medium-sized hydrophotovoltaic hybrid energy systems considering multiple uncertainties. J. Clean. Prod. 276, 1–14.

YW. Yuan, Z. Liu, C. Su, X. Wang, "Photovoltaic capacity optimization of small and medium-sized hydro photovoltaic hybrid energy systems considering multiple uncertainties," in J. Clean. Prod.,vol.276, pp.1-14, Sept.